UNIVERSITÀ DEGLI STUDI DI PADOVA
DIPARTIMENTO DI FISICA E ASTRONOMIA
CORSO DI LAUREA MAGISTRALE IN FISICA

QUANTIFYING DRY MERGER EFFECTS ON THE GROWTH OF MASSIVE COMPACT GALAXIES: DEPENDENCY ON THE SÉRSIC INDEX

Relatore:
Prof. Enrico Maria Corsini
Correlatore:
Prof. Marc Balcells

Laureando:
Matteo Frigo

Anno accademico 2013/2014

Contents

1 Introduction

Galaxy morphology is a powerful tool for studying the secular processes that act on galaxies. Section 1.1 discusses morphological classification and its importance in the study of galaxies. Section 1.2 focuses on elliptical galaxies, which are the object of study of this thesis, and summarizes their main properties. Section 1.3 describes the aims of the thesis and its structure.

1.1 Morphology and evolution of galaxies

The classification of galaxies according to their morphology is older than the concept of galaxy itself, yet it is still very relevant today in the study of their formation and evolution. Herschel (1864) was the first to systematically search the sky for weirdly shaped *nebulae* and roughly classify them according to their size, shape, brightness, and central concentration. The study of galactic morphology however took off with the improvements of telescopes and photography which underwent in the late 19th century. They allowed astronomers to resolve and recognize details in galactic structure such as spiral arms, bars, and dust lanes. With this newer technology several nebulae were found to have a spiral structure. Among them was also the Andromeda nebula (M31), the spiral structure of which was discovered by Roberts (1893). Further improvements allowed Curtis (1918) to identify a new category of nebulae, the so-called ϕ-type spirals, which are known today as barred spirals. Curtis argued that all nebulae were in fact spirals, and that those who did not look like they were would have been discovered as such in the future, with improved instrumentation. Hubble (1922) instead argued correctly that some nebulae had indeed a non-spiral shape. At the same time was going on what became known as the *great debate* between Shapley and Curtis about whether spiral nebulae were part of the Milky Way or external objects. The debate was ended by Hubble (1925), who through the study of cepheid variable stars came to the conclusion that M31 and the other spiral nebulae were in fact separate galaxies. Hubble (1926) also published a new classification system to catalog all the known galaxies at the time. This new system, known today as the *Hubble sequence*, distinguishes elliptical (E), spiral (S) or barred spiral (SB) galaxies. The ellipticals are further categorized with a number that expresses their ellipticity: E0, E1,..., En, where $n \simeq 10\,e$ and e is the apparent ellipticity of the galaxy. The spirals are instead categorized with a letter, a,b or c, according to the shape of their bulges and spiral arms:

Sa/SBa have a pronounced bulge and tightly-wound smooth arms, while Sc/SBc are flatter and have a fainter bulge, as well as loosely-wound spiral arms which can be resolved in star clusters. All these categories were shown in a continuous sequence that began with circular ellipticals (E0), went on to flattened ellipticals (E1-E7) and then divided into two branches, one for normal spirals and one for barred spirals (Figure 1). The only missing link in this sequence was between the most flattened ellipticals (E7) and the most bulgy spirals (Sa/SBa). Hubble hypothesized the existence of a galaxy type that would fill that place in the sequence, shaped like a disk but without a spiral structure. He designated this new type of galaxy as S0, and objects of this type were later found to really exist. Irregular galaxies (Ir) have also been later added, this time at the end of the spiral side, completing thus the sequence as it is usually represented today.

The Hubble sequence has been the framework through which the morphology of galaxies has been organized ever since, but a lot of modifications have also been proposed to it. Sandage (1961, 1994) suggested what is now known as the *revised Hubble-Sandage system*, which subdivided the S0 galaxies in different varieties and proposed a more complicated version of Hubble's "tuning fork" sequence. Morgan (1958) introduced the cD type of galaxies, giant ellipticals found in the center of galaxy clusters, with extremely extended light distribution. De Vaucouleurs (1959) suggested that spiral galaxies should also be distinguished based on the presence of lenses and rings. Van der Bergh (1976) proposed that S0 galaxies should not be the connection between ellipticals and spirals, but should instead form a branch on their own, parallel to the spiral one. Kormendy & Bender (1996) argued that the classification of elliptical galaxies according to their apparent flatness is not physically relevant. Therefore they modified the elliptical branch of the Hubble sequence by distinguishing instead "boxy" and "disky" ellipticals based on the shape of their isophotes.

The reason why morphology is still relevant today is that it gives us a key to understand the formation and evolution of galaxies. Galaxies with a similar morphology might represent two successive steps in the same galaxy evolution pattern, or could represent two parallel and separate paths of evolution, but in both cases morphology gives us a framework to better understand the processes they undergo. An example of this is the so called *morphology-density relation*, which is the fact that elliptical and S0 galaxies are far more common in dense galaxy clusters, while spirals and irregulars are more common in the field, where the density of galaxies is much lower (Dressler 1980). This

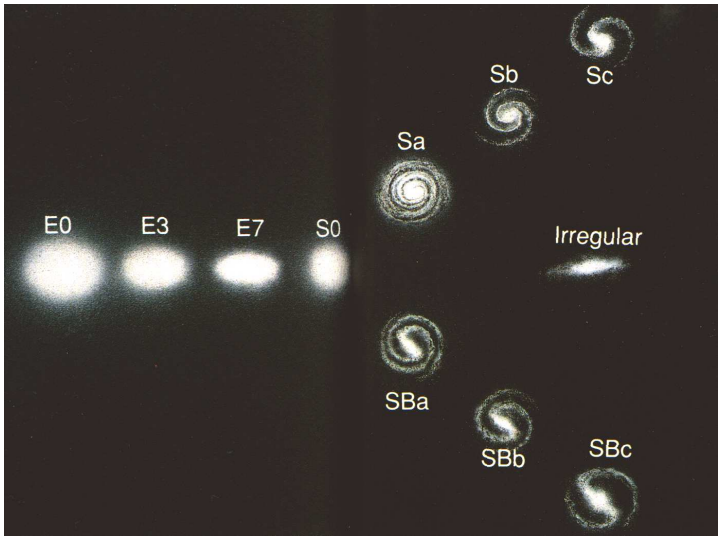

Figure 1: The morphological sequence of galaxies proposed by Hubble.

could both indicate that elliptical galaxies tend to form in higher density environments and/or that spiral galaxies which ended up in such environments lose their gas and spiral structure to become S0 galaxies. Similarly, different morphological classes have been shown to relate to different stellar populations: elliptical and S0 galaxies, also known as *early-type galaxies*, mostly have old stars and are very poor in gas, while spirals and irregulars, or *late-type galaxies*, are rich in gas, and therefore have a lot of star forming regions and a younger stellar population, suggesting they formed later. We also observe a correlation with redshift, and therefore with the look-back time: galaxies that are further away tend to be smaller, less symmetric and more irregular, suggesting that they are still undergoing processes of evolution. In general, studying the morphology of galaxies and its correlation with their observable properties is extremely useful to understand their formation and evolution. Another example of this comes from the E-E dichotomy between boxy and disky elliptical galaxies introduced previously. Compared to disky ellipticals boxy ellipticals are more luminous and massive, have less rotation, more anisotropic velocity dispersion, a significantly older stellar population and a higher presence of α elements (Mg, Si, Ca,...). α elements are mostly produced by type II supernovae, that happen especially during rapid star formation processes. These clues suggest that the two types of ellipticals

have a different origin: boxy ellipticals might have formed by rapid collapse in the center of galaxy clusters and later evolved by dry mergers with smaller galaxies, while disky ellipticals might have originally been late-type galaxies with a disk shape, young stars and high rotation, which got transformed into their present form by interaction with the environment, for instance by entering a galaxy cluster (Kormendy et al. 2008).

1.2 Elliptical galaxies

Elliptical galaxies are particularly interesting for the study of formation and evolution of galaxies because their history reflects conditions of both early cosmological times, when they initially formed, and recent ones, when they underwent several mergers with smaller galaxies to reach their current shape. They are the galaxy type which varies the most in mass, brightness, and size, and they come in a few different subclasses (e.g., Carroll & Ostlie 1996):

- *Normal elliptical galaxies* (E) are generally very bright objects and have mass between 10^8 and $10^{13}\,\mathrm{M}_\odot$, absolute blue magnitude between -15 and -23, diameter between less than 1 and 200 kpc. Their mass-to-light ratio, the ratio between the total mass of the galaxy and its luminosity, can vary between 7 and $100\,\mathrm{M}_\odot/\mathrm{L}_\odot$.

- *cD galaxies*, the giant ellipticals found at the center of galaxy clusters, can have mass up to $10^{14}\,\mathrm{M}_\odot$ and mass-to-light ratio up to $750\,\mathrm{M}_\odot/\mathrm{L}_\odot$. They have a very bright central region and are very extended in the outer parts, reaching up to 1 Mpc in diameter.

- *Dwarf elliptical galaxies* (dE) have significantly lower surface brightness than normal ellipticals with the same absolute magnitude. They can range in mass between 10^7 and $10^9\,\mathrm{M}_\odot$ and in absolute blue magnitude between -13 and -19. Their mass-to-light ratio is about $10\,\mathrm{M}_\odot/\mathrm{L}_\odot$ and their diameter is in the order of 1 kpc.

- *Blue compact dwarves* (BCD) are unusually blue dwarf ellipticals with young stars and a lot of gas. Their mass-to-light ratio is remarkably

low, as much as $0.1\,\mathrm{M}_\odot/\mathrm{L}_\odot$.

- *Dwarf spheroidal galaxies* (dSph) are the smallest and least luminous elliptical galaxies, with absolute blue magnitudes as low as -8 and diameter between 0.1 and 0.5 kpc.

1.2.1 Surface brightness

One of the most important ways to characterize an elliptical galaxy is by describing its surface brightness, or more specifically the dependence of surface brightness on the distance from the galactic center r. De Vaucouleurs (1953) showed that the dependency on r of the surface brightness of most giant elliptical galaxies can be well approximated by the law:

$$I(r) = I_\mathrm{e} \exp(-k((r/r_\mathrm{e})^{1/4} - 1)) \tag{1}$$

where r_e is the effective radius, the radius inside which lies half of the light of the galaxy, and k is a constant. More recently it has been shown (Caon et al. 1993) that the profile proposed by Sérsic (1963) better describes a wider range of elliptical galaxies, including the small ones. The Sérsic profile, or Sérsic law, resembles the de Vaucouleurs law but replaces the exponent 4 with a new parameter n, the Sérsic index, and has the following expression:

$$I(r) = I_\mathrm{e} \exp(-b_n((r/r_\mathrm{e})^{1/n} - 1)) \tag{2}$$

where b_n is a parameter that depends on n. This equation has 3 free parameters, I_e, r_e and n, compared to the 2 free parameters of the de Vaucouleurs law, and reduces to it when $n = 4$. Ellipticals with larger mass and size are better described by the Sérsic profile with $n \geq 4$, while smaller ellipticals have Sérsic indices around 1 or 2. This means that they are less concentrated in the center. This distinction also correlates with the one between boxy and disky ellipticals: boxy ellipticals tend to have $n > 4$, whereas disky ellipticals have $n \simeq 3$ (Kormendy et al. 2008). Fitting of the surface brightness profile of observed galaxies with a Sérsic law is thus very common, and the obtained parameters are used to characterize them. It is interesting how elliptical galaxies that dramatically differ in size, luminosity, and formation history have a surface brightness profile that can be described by the same formula,

by varying a simple parameter. This tells us that similar processes must be in act on all elliptical galaxies. However, the different Sérsic indices, as well as deviations from the Sérsic law, might be even more important. They are a powerful tool to study the formation of these galaxies.

1.2.2 Dynamics

Elliptical galaxies can also be studied through their internal dynamics. The average line-of-sight velocity of stars V can be directly measured by spectroscopical analysis of absorption lines in their light. However, since in elliptical galaxies the stars move in very different and uncorrelated orbits, it is often more meaningful to characterize them with the velocity dispersion σ, which is the statistical dispersion of velocities about the average in that part of the galaxy. In elliptical galaxies usually $\sigma >> V$, especially in the case of boxy ellipticals. This means that they are sustained by dynamical pressure, rather than rotation, as is the case for disky ellipticals. It also means that the flattening of some boxy elliptical galaxies can not be attributed to their rotation. The spectroscopical analysis of starlight allows us to trace σ up to $2r_{\mathrm{e}}$. To be able to measure it further from the center it is necessary to use as tracers planetary nebulae or globular clusters, whose orbits reach further outside in the halo of the galaxy. These velocity measurements of matter in the outskirts of the galaxy allow us to deduce the strenght of the gravitational field that moves this matter, and thus to calculate the mass which generates the field, the *dynamical mass* of the galaxy. Although different methods obtain different estimates, all the measurements show that the dynamical mass is much bigger than the observable luminous mass, having often mass to light ratios of at least 50 (e.g., Gerhard 2006). This means that elliptical galaxies must have very massive dark matter halos surrounding them, like all other galaxies. These measurements also show that some elliptical galaxies have considerable rotation in the outer parts. Several computational studies (e.g., Barnes & Efstathiou 1987; Bullock et al. 2001) have related this high angular momentum to their formation history, arguing that major mergers cause these very high velocities, while mergers with minor satellites leave the galaxy with negligible rotation speed.

1.2.3 The fundamental plane

It has been shown that all the characteristic quantities that describe elliptical galaxies can be related by an equation known as the *fundamental plane* of elliptical galaxies (Djorgovski & Davis 1987; Dressler et al. 1987):

$$\log r_{\rm e} = 2\log\sigma - \log I_{\rm e} - \log(M_{\rm e}/L_{\rm e}) + C \tag{3}$$

where $I_{\rm e}$ and $M_{\rm e}/L_{\rm e}$ are respectively the average surface brightness and the mass-to-light ratio inside $r_{\rm e}$ and C is a constant. This equation comes directly from a theoretical principle, the virial theorem, which in the case of elliptical galaxies takes the form:

$$\sigma^2 \propto \frac{G\,M_{\rm e}}{r_{\rm e}} \simeq \frac{G\,(M_{\rm e}/L_{\rm e})\,(I_{\rm e}{r_{\rm e}}^2)}{r_{\rm e}}. \tag{4}$$

Taking the logarithm we obtain the fundamental plane equation. If the mass-to-light ratio is assumed constant, it can be seen as the equation of a plane in the $\sigma, r_{\rm e}, I_{\rm e}$ space, hence the name of this correlation. The fact that elliptical galaxies seem to be correctly described by it tells us that gravity is indeed the main player in the formation and evolution of galaxy. However, deviations from the fundamental plane have been found. For instance, it has been found that the plane is tilted, suggesting that the mass-to-light ratio varies with the total mass of the galaxy (Bernardi et al. 2003). These deviations can tell us a lot about the secular evolution of elliptical galaxies and how it differs in different ranges of mass and size, and can give us insights on the role of secondary factors in these processes, such as gas friction and feedback of an active galactic nucleus.

1.3 Aim and outline of the thesis

One way of studying how the observable properties of elliptical galaxies relate to their formation history is by comparing them with theoretical models. A lot of effort has been put into studying the dynamics of stable gravitationally bound systems from an analytical point of view. However, complex dynamic processes such as mergers and interaction with the environment can only be modeled and studied through numerical simulations. Simulations are also needed to study the structure and evolution of dark matter halos, which otherwise can be observed only indirectly and not in detail. To carry out simulations of these processes, we first need to be able to generate stable

models of elliptical galaxies, and this can be done with numerical codes that implement the aforementioned analytical studies on stable gravitational systems. One such code is the one by Smulders (1995), written as his master thesis project. It builds stable models of elliptical galaxies that emulate the de Vaucouleurs law. These models have two components, a luminous matter spheroid and a dark matter halo, and the code allows the user to choose the mass and size ratio of the two and the degree of anisotropy. The Smulders code has been adopted in several papers, such as González-García & van Albada (2003) and Tapia et al. (2013). However, due to the limitations of the de Vaucouleurs law, a code to model ellipticals with any Sérsic index was needed. This is particularly true when wanting to study the secular processes acting on elliptical galaxies through the dependence on their Sérsic index. The first part of the work described in this thesis consisted therefore in writing a new code, based on the Smulders code, that generates models of galaxies with surface brightness following the Sérsic law, and with better accuracy and versatility than the original code.
The outline of the thesis is the following:

- Chapter 2 presents the theoretical basis for the construction of stable two-component models of elliptical galaxies and derives the main equations used in the code.

- Chapter 3 discusses the empirical laws for fitting the surface brightness profiles of galaxies and their deprojection into tridimensional density profiles, presenting in detail the ones which the code is trying to recreate.

- Chapter 4 explains the numerical methods used to implement all these features in a N-body simulation.

- Chapter 5 presents the various options available in the code and analyze the models generated from it, in particular their faithfulness to the desired density profiles and their stability.

- Chapter 6 shows an application of the code to an actual astrophysical problem: a simulation of the growth of two elliptical galaxies through minor mergers, with the objective of understanding if and how the evolution of elliptical galaxies depends on their initial Sérsic index.

- Chapter 7 gives a summary and the conclusions of the thesis.

The work on the code and on the simulations has been carried out at the Instituto de Astrofísica de Canarias in San Cristóbal de La Laguna (Tenerife, Spain) and at the Isaac Newton Group of Telescopes (La Palma, Spain), under the supervision of prof. Marc Balcells. A scientific paper on this work is also expected to be completed and published in late 2014.

2 Galactic dynamics

Over the last century the dynamics of stellar systems have been studied in great detail (see Binney & Tremaine 1987 for an extensive review). This chapter presents some of the results derived for the particular case of *collisionless* systems. Section 2.1 gives a definition of collisionless stellar dynamics and derives its fundamental equation, the collisionless Boltzmann equation. In Section 2.2 is derived the Jeans theorem, which under certain conditions allows us to describe the dynamics of a stellar system solely by its energy and angular momentum. Finally, Section 2.3 derives the formula used in the code for calculating the distribution function of the system from its density and potential radial profiles.

2.1 Collisionless Boltzmann equation

A complete analytical description of a gravitational system with billions of independent objects (like stars and/or dark matter particles) is clearly not feasible, but many of its properties can still be understood by using an approximation. This basic assumption is that, instead of considering the interactions between each star and every other, each star feels a smooth galactic potential Φ that is related to the (smoothed) local star density ρ through the Poisson equation:

$$\nabla\Phi(\mathbf{x}) = -4\,\pi\,G\,\rho(\mathbf{x}). \tag{5}$$

Contributions of close two-body interactions on the motion of stars are thus not considered. Each star interacts only with the galaxy, as if the star system was a perfect fluid moving in the galactic potential generated by itself. This assumption holds well when the density of stars is very low relatively to the size of the system. This is the case of a galaxy, but might not work as well when dealing with more compact systems such as globular clusters. Theoretical models which follow this assumption are called *collisionless*.

Now that the system we are studying is defined, we need to be able to describe it quantitatively and to derive the equation for its evolution over time. In general, a gravitational system is completely determined by knowing the positions and velocities of all of its stars at a given time. Therefore, a complete description of the system is given by the *distribution function* or *phase-space density*, $f(\mathbf{x}, \mathbf{v}, t)$. This is defined as the number of stars having position in the small volume $d^3\mathbf{x}$ centered in $\mathbf{x}$ and velocity in the range $d^3\mathbf{v}$

centered in $\mathbf{v}$, at the time t. It satisfies $f(\mathbf{x}, \mathbf{v}, t) \geq 0 \; \forall \mathbf{x}, \mathbf{v}, t$, and it is usually defined to be 1:

$$\int f(\mathbf{x}, \mathbf{v}, t) \, d^3\mathbf{x} \, d^3\mathbf{v} \, dt = 1. \tag{6}$$

It can also be convenient to describe positions and velocities of the stars in a single joint variable $\mathbf{w}$, defined as:

$$\mathbf{w} = (\mathbf{x}, \mathbf{v}) = (w_1, w_2, w_3, w_4, w_5, w_6). \tag{7}$$

Newton equation assures that the future and past evolution of a system is completely determined as soon as the system is determined at any given time by its distribution function $f(\mathbf{w}, t)$. For each single particle they are:

$$\dot{\mathbf{w}} = (\dot{\mathbf{x}}, \dot{\mathbf{v}}) = (\mathbf{v}, -\nabla\Phi) \tag{8}$$

but what we want is an equation for the distribution function itself. The time evolution of the distribution function is given by the Liouville theorem, which under very general assumptions states that:

$$\frac{df}{dt} = 0. \tag{9}$$

It can be obtained by considering the system like a fluid moving smoothly in the 6-dimensional phase space. If in fact we consider a small 6-dimensional volume in the phase space, the variation of its total mass is given by the amount of mass which has escaped or entered the 6-dimensional volume:

$$\frac{dM}{dt} = -\int_S f(\mathbf{w}) \dot{\mathbf{w}} \, d^5S. \tag{10}$$

From the definition of the distribution function, the first member is equal to:

$$\frac{dM}{dt} = \frac{d}{dt} \int f(\mathbf{w}, t) d^6\mathbf{w} = \int \frac{df}{dt}(\mathbf{w}, t) d^6\mathbf{w} \tag{11}$$

and by using the divergence theorem, it results that the second member is equal to:

$$\int_S f(\mathbf{w}) \dot{\mathbf{w}} d^5S = -\int_V \nabla_{\mathbf{w}} \cdot (f(\mathbf{w}, t) \dot{\mathbf{w}}) \, d^6\mathbf{w}. \tag{12}$$

Putting Equations (11) and (12) together we obtain a continuity equation for the phase-space density:

$$\int_V \frac{\partial f}{\partial t}(\mathbf{w}, t) \, d^6\mathbf{w} + \int_V \nabla_{\mathbf{w}} \cdot (f(\mathbf{w}, t) \dot{\mathbf{w}}) \, d^6\mathbf{w} = 0 \tag{13}$$

or equivalently:

$$\frac{\partial f}{\partial t}(\mathbf{w},t) + \nabla_{\mathbf{w}} \cdot (f(\mathbf{w},t)\dot{\mathbf{w}}) = 0. \tag{14}$$

In addition, the star fluid which we are describing has a very special property:

$$\nabla_{\mathbf{w}} \cdot \dot{\mathbf{w}} = \sum_{\alpha=1}^{6} \frac{\partial \dot{w_\alpha}}{\partial w_\alpha} = \sum_{i=1}^{3} (\frac{\partial v_i}{\partial x_i} + \frac{\partial \dot{v_i}}{\partial v_i}) = -\sum_{i=1}^{3} \frac{\partial}{\partial v_i}\frac{\partial \Phi}{\partial x_i} = 0 \tag{15}$$

where $\frac{\partial v_i}{\partial x_i} = 0$ because x_i and v_i are independent variables in the phase space and $\frac{\partial}{\partial v_i}\nabla\Phi = 0$ because the potential does not depend on velocities. This means that Equation (14) can be rewritten as:

$$\frac{\partial f}{\partial t} + \nabla_w f \cdot \dot{\mathbf{w}} = 0 \tag{16}$$

which is completely equivalent to the Liouville equation (Equation (9)). In our case we can substitute $\dot{\mathbf{v}} = -\nabla\Phi$, and therefore, separating positions and velocities we obtain the *collisionless Boltzmann equation*:

$$\frac{\partial f}{\partial t} + \nabla_x f \cdot \mathbf{v} - \nabla_v f \cdot \nabla_x \Phi = 0. \tag{17}$$

This is the fundamental equation of *collisionless stellar dynamics*, and it describes the evolution over time of the distribution function of the system. It might be noted that if collisions were included it would not be true that $\nabla_{\mathbf{w}} \cdot \dot{\mathbf{w}} = 0$, and therefore the equation for the distribution function would have an additional term. Up until now we defined f as the number of stars per phase-space volume, but it can also be interpreted as the luminosity density or mass density, when the stars have the same luminosity or mass. Otherwise, a different collisionless Boltzmann equation should be used for each type of star.

The equation also holds true in any canonical coordinate system. If in fact we define a new coordinate system $\mathbf{W} = (W_1, W_2, W_3, W_4, W_5, W_6)$, with differential $d^6\mathbf{W}$, the phase-space density $F(\mathbf{W},t)$ in this system of coordinates must be related to the old one by

$$F(\mathbf{W},t)d^6\mathbf{W} = f(\mathbf{w},t)d^6\mathbf{w}. \tag{18}$$

It can now be shown (see Binney & Tremaine 1987, Appendix 1-D) that in the case of canonical coordinates the 6-dimensional phase-space volume does

not depend on the chosen set of coordinates, $d^6\mathbf{W} = d^6\mathbf{w}$, therefore it must be:

$$F(\mathbf{W}, t) = f(\mathbf{w}, t). \tag{19}$$

The distribution function is the same in every set of coordinates, which means that the collisionless Boltzmann equation also holds true for any given set of canonical coordinates.

2.2 Jeans theorem

An integral of motion is defined as a function $I(\mathbf{x}, \mathbf{v})$ of the canonical coordinates which satisfies:

$$\frac{d}{dt} I(\mathbf{x}, \mathbf{v}) = 0. \tag{20}$$

Using the equations of motion however, this means that

$$0 = \frac{dI}{dt} = \frac{\partial I}{\partial t} + \nabla_x I \cdot \dot{\mathbf{x}} + \nabla_v I \cdot \dot{\mathbf{v}} = \frac{\partial I}{\partial t} + \nabla_x I \cdot \mathbf{v} + \nabla_v I \cdot \nabla_x \Phi. \tag{21}$$

This means that any integral of motion, or any function of integrals of motion, satisfies the collisionless Boltzmann equation, which is the basis of the *Jeans theorem*: Any steady-state solution of the collisionless Boltzmann equation depends on the phase-space coordinates only through integrals of motion, and any function of integrals of motion yields a steady-state solution of the collisionless Boltzmann equation.
What has already been shown already proves the first part of the theorem: if f satisfies the collisionless Boltzmann equation it is also an integral of motion. If instead $f(I_1, I_2, ..., I_n)$ is a function of the integrals of motion $I_1(\mathbf{x}, \mathbf{v}), ..., I_n(\mathbf{x}, \mathbf{v})$, then

$$\frac{d}{dt} f(I_1, I_2, ..., I_n) = \sum_{i=1}^{n} \frac{\partial f}{\partial I_i} \frac{dI_i}{dt} = 0 \tag{22}$$

because $dI_i/dt = 0$ by definition of integral of motion. The condition $df/dt = 0$ is equivalent to the collisionless Boltzmann equation, therefore, we have proven that it is satisfied by any function of integrals of motion.
However, this theorem is not enough for our purposes, what we need is the *strong Jeans theorem*: The distribution function of a steady-state galaxy in which almost all orbits are regular with incommensurable frequencies may

be presumed to be a function of only three isolating integrals.
Any observable Q of the system must have the form:

$$\langle Q(t)\rangle = \int Q(\mathbf{x},\mathbf{v}) f(\mathbf{x},\mathbf{v},t)\, d^3\mathbf{x}\, d^3\mathbf{v}. \tag{23}$$

Since the galaxy is in steady-state this average does not depend on time, and it is also equal to its time average:

$$\langle Q\rangle = \overline{\langle Q\rangle} = \frac{1}{T}\int_0^\infty \langle Q\rangle\, dt = \int Q(\mathbf{x},\mathbf{v})\, \overline{f}(\mathbf{x},\mathbf{v})\, d^3\mathbf{x}\, d^3\mathbf{v} \tag{24}$$

where

$$\overline{f}(\mathbf{x},\mathbf{v}) \equiv \frac{1}{T}\int_0^\infty f(\mathbf{x},\mathbf{v},t)\, dt. \tag{25}$$

Since f satisfies the collisionless Boltzmann equation, $df/dt = 0$, we can write:

$$f(\mathbf{x},\mathbf{v},t) = f(\mathbf{x}_t,\mathbf{v}_t,0) \tag{26}$$

where $(\mathbf{x}_t,\mathbf{v}_t)$ are the positions and velocities at time $t=0$ of the particles that at time t would have been in $(\mathbf{x},\mathbf{v})$. Now, if the orbits are regular we can use the action-angle coordinates, $(\theta,\mathbf{J})$, which are canonical and do not change the distribution function. Using the canonical equations, the frequencies are:

$$w_i = \dot{\theta}_i = \frac{\partial H}{\partial J_i} \tag{27}$$

which are constant, since the actions J_i are integrals of motion. We thus have $\theta_i(t) = \theta_i(0) + \omega_i t$ and we can write:

$$\begin{aligned}\overline{f}(\mathbf{x},\mathbf{v}) = \frac{1}{T}\int_0^\infty f(\mathbf{x}_t,\mathbf{v}_t,0)\, dt &= \frac{1}{T}\int_0^\infty f(\mathbf{J}_t,\theta_t,0)\, dt \\ &= \frac{1}{T}\int_0^\infty f(\mathbf{J},\theta-\omega t,0)\, dt.\end{aligned} \tag{28}$$

We can now apply the *time averages theorem*, which states that if the frequencies ω are incommensurable, the average time spent by the phase-space point of a star (on regular orbit) in a region D is proportional to $V(D) = \int_D d^3\theta$ through D (see Binney & Tremaine 1987, Chapter 3.5). Because of this, we can write the averaging over time as an averaging over angles:

$$\overline{f}(\mathbf{J}) = \frac{1}{(2\pi)^3}\int f(\mathbf{J},\theta) d^3\theta \tag{29}$$

This distribution function does not depend on the angles, but depends only on the three actions J_i. It is equivalent to the original distribution function of the system, because from what we have shown:

$$\langle Q(t) \rangle = \int Q(\mathbf{x}, \mathbf{v}) \overline{f}(\mathbf{J}(\mathbf{x}, \mathbf{v}))\, d^3\mathbf{x}\, d^3\mathbf{v}. \tag{30}$$

This means that we can adopt $\overline{f}$ as the distribution function of the system, and since the actions can be expressed as a combination of any three isolating integrals of motion we have proven the theorem.
The importance of the strong Jeans theorem is that it allows us to use a distribution function that only depends on the total energy of the particles E and on the angular momentum $\mathbf{J}$. In particular, in the case of spherical systems the distribution function can depend on the angular momentum only through its magnitude, and therefore our distribution function will be simply defined as $f(E, J)$.

2.3 Deriving the distribution function from the density profile

The models of galaxies generated by this code follow specific mass density profiles, and their potentials are easily obtained through the Poisson equation. The distribution function of the models however needs to be calculated from these density-potential pairs, so that the galaxy remains stable. In the following discussion it is useful to define the *relative potential* Ψ and the *relative energy* $\mathcal{E}$:

$$\Psi \equiv -\Phi + \Phi_0 \tag{31a}$$

$$\mathcal{E} \equiv -E + \Phi_0 = \Psi - \frac{1}{2}\, v^2 \tag{31b}$$

where Φ_0 is an arbitrary value, chosen so that the distribution function is positive for every $E \geq 0$ and 0 for every $E < 0$.

2.3.1 Isotropic models

If the model we want to generate is isotropic, the distribution function is further reduced, and it depends only on the energy: $f = f(\mathcal{E}) = f(\Psi - \frac{1}{2}v^2)$.

In this case, the velocity dispersion in any direction i ($i = r$, θ or ϕ) is:

$$\overline{{v_i}^2} = \frac{1}{\rho} \int {v_i}^2 \, f(\Psi - \frac{1}{2}({v_r}^2 + v_\theta^2 + v_\phi^2)) \, dv_r \, dv_\theta \, dv_\phi \tag{32}$$

and we have $\overline{{v_r}^2} = \overline{{v_\theta}^2} = \overline{{v_\phi}^2}$. If instead the distribution function also depends on J we have $\overline{{v_r}^2} \neq \overline{{v_\theta}^2} = \overline{{v_\phi}^2}$ and the model is anisotropic.
The spatial density of stars, depends on the distribution function through:

$$\rho(r) = \int f(\Psi - \frac{1}{2}v^2) \, d^3\mathbf{v} = 4\,\pi \int f(\Psi - \frac{1}{2}v^2) \, v^2 \, dv \tag{33}$$

and changing variable to $\mathcal{E} = \Psi - \frac{1}{2}v^2$ we have:

$$\rho(r) = 4\,\pi \int_0^\Psi f(\mathcal{E}) \, \sqrt{2(\Psi - \mathcal{E})} \, d\mathcal{E}. \tag{34}$$

Differentiating both sides with respect to Ψ and dividing by $2\sqrt{2}\,\pi$ we obtain:

$$\frac{1}{2\sqrt{2}\,\pi} \, \frac{d\rho}{d\Psi} = \int_0^\Psi \frac{f(\mathcal{E}) d\mathcal{E}}{\sqrt{\Psi - \mathcal{E}}}. \tag{35}$$

This expression is an Abel integral[1], and therefore it can be inverted to get:

$$f(\mathcal{E}) = \frac{1}{2\sqrt{2}\,\pi^2} \frac{d}{d\mathcal{E}} \int_0^\mathcal{E} \frac{d\rho}{d\Psi} \, \frac{1}{\sqrt{\Psi - \mathcal{E}}} \, d\Psi. \tag{37}$$

Expliciting the derivative we finally obtain *Eddington's formula*:

$$f(\mathcal{E}) = \frac{1}{2\sqrt{2}\,\pi^2} \left(\int_0^\mathcal{E} \frac{d^2\rho}{d\Psi^2} \, \frac{1}{\sqrt{\Psi - \mathcal{E}}} \, d\Psi + \frac{1}{\sqrt{\mathcal{E}}} \left(\frac{d\rho}{d\Psi} \right)_{\Psi=0} \right). \tag{38}$$

This formula gives us the distribution function for any density-potential pair. It is worth noting that these density and potential do not have to be related by the Poisson equation; the formula simply calculates the distribution function

[1] An integral of the form $f(x) = \int_0^x \frac{g(y)dy}{(x-y)^\alpha}$ with $0 < \alpha < 1$ is an Abel integral, and it can be inverted to obtain:

$$g(y) = \frac{\sin(\pi\alpha)}{\pi} \frac{d}{dx} \int_0^y \frac{f(x)}{(y-x)^{1-\alpha}} dx. \tag{36}$$

for particles distributed according to a given density and immersed in a given potential. This is critical to build models with multiple components, such as the ones built by the code, because each component has an independent density profile but feels the same potential, the one generated by all the components. The second term of the equation is equal to zero when the mass of the system is limited, therefore the equation that will be used in the code is simply:

$$f(\mathcal{E}) = \frac{1}{2\sqrt{2}\pi^2} \left(\int_0^{\mathcal{E}} \frac{d^2\rho}{d\Psi^2} \frac{1}{\sqrt{\Psi - \mathcal{E}}} \, d\Psi \right). \tag{39}$$

This integral can be calculated analitically in the case of a simple Jaffe model (see Section 3.1), but not if there are other components (such as the dark matter halo). In the case of the Prugniel-Simien profile (see Section 3.4), even with a single component model it's not possible to obtain an analytic solution. In all these cases, the integral has to be calculated numerically. Section 4.3 will show how the integration is done in the code.

2.3.2 Anisotropic models

In the spherical anisotropic case the distribution function must also depend on the angular momentum: $f = f(\mathcal{E}, J)$. Because of this, to get the density $\rho(r)$ from the distribution function we also have to integrate (non trivially) over the angles:

$$\begin{aligned} \rho(r) = \int f(\mathcal{E}, J) \, d^3\mathbf{v} = \\ = 2\,\pi \int_0^{\pi} \sin(\eta) \, d\eta \int_0^{\infty} f\left(\Psi - \frac{v^2}{2}, |r\, v\, \sin(\eta)|\right) v^2 \, dv \end{aligned} \tag{40}$$

where η is the angle between $\mathbf{r}$ and $\mathbf{v}$ ($J = |\mathbf{r} \times \mathbf{v}| = r\, v\, \sin\eta$).
There are now various ways of constructing an anisotropic model extending an isotropic one, but the way used in the code is the one by Osipkov (1979) and Merrit (1985). It consists in defining the distribution function not as a simple function of the energy but as function of a quantity that depends on both the energy and the angular momentum,

$$Q = \mathcal{E} + \frac{J^2}{2r_{\rm a}} = \Psi - \frac{1}{2}v^2 \left(1 - \frac{r^2}{r_{\rm a}^2} \sin^2(\eta)\right). \tag{41}$$

Doing the same steps as in the isotropic case, we can change the variable of integration in Equation (40) to Q ($dQ = -(1 + (r/r_\mathrm{a})^2 \sin^2(\eta))vdv$), obtaining:

$$\rho(r) = 2\pi \int_0^\pi \sin(\eta) d\eta \int_0^\Psi f(Q) \frac{\sqrt{2(Q-\Psi)}}{(1 - (\frac{r}{r_\mathrm{a}})^2 \sin^2(\eta))^{\frac{3}{2}}} dQ. \tag{42}$$

Integrating first over the angles we have:

$$\int_0^\pi \frac{\sin(\eta)}{(1 - (\frac{r}{r_\mathrm{a}})^2 \sin^2(\eta))^{\frac{3}{2}}} \, d\eta = \frac{2}{1 + (\frac{r}{r_\mathrm{a}})^2} \tag{43}$$

and therefore:

$$\left(1 + \frac{r^2}{{r_\mathrm{a}}^2}\right) \rho(r) = 4\,\pi \int_0^\Psi f(Q)\, \sqrt{2(Q-\Psi)}\, dQ. \tag{44}$$

This equation is exactly equivalent to Equation (34) if we define:

$$\rho_Q(r) = \left(1 + \frac{r^2}{{r_\mathrm{a}}^2}\right) \rho(r). \tag{45}$$

By analogy with the isotropic case we can therefore conclude that:

$$f(Q) = \frac{1}{2\sqrt{2}\,\pi^2} \left(\int_0^Q \frac{d^2\rho_Q}{d\Psi^2} \frac{1}{\sqrt{\Psi - Q}}\, d\Psi + \frac{1}{\sqrt{Q}} \left(\frac{d\rho_Q}{d\Psi}\right)_{\Psi=0} \right). \tag{46}$$

In other words, we can use the Eddington formula of the isotropic case by substituting $\mathcal{E}$ with $Q = \mathcal{E} + J^2/2r_\mathrm{a}$ and ρ with $\rho_Q = (1 + (r/r_\mathrm{a})^2)\rho$. r_a is the *anisotropy radius*, and its absolute value corresponds approximately to the radius from which anisotropy effects become dominant. If $r_\mathrm{a} > 0$ the model is radially anisotropic, and orbits beyond $r = r_\mathrm{a}$ are almost radial. If instead $r_\mathrm{a} < 0$ the model is tangentially anisotropic, and orbits beyond $r = -r_\mathrm{a}$ are almost circular. When $r_\mathrm{a} \to \pm\infty$ the anisotropic model reduces to an isotropic one.

3 Density profiles

This chapter presents some of the empirical laws that are used to model the radial profiles of surface brightness and mass density in observed elliptical galaxies. Section 3.1 presents the de Vaucouleurs and Sérsic laws for the surface brightness. Sections 3.2, 3.3, and 3.4 present the Jaffe, Hernquist and Prugniel-Simien profiles, respectively, which are mass density profiles. These profiles are particularly relevant in this thesis because they are the blueprint through which the code creates models of galaxies.

3.1 De Vaucouleurs law and Sérsic law

The formulae in Section 2.3 allow us to calculate the distribution function that makes an elliptical galaxy stable. However, they depend on the radial profile of the density $\rho(r)$ and of the potential $\Phi(r)$, where r is the distance from the center. While the potential radial profile can be calculated from the density radial profile using the Poisson equation, the latter has to be modeled from observational data. In fact being a tridimensional quantity it cannot be observed directly, but it can be derived from the surface-brightness radial profile, which is proportional to its projection along the line of sight. The surface-brightness profiles of elliptical galaxies have been studied since the 1930s. It has been shown (de Vaucouleurs 1948, 1953) that the empirical law, known as the *de Vaucouleurs law*, represents quite accurately the surface brightness profile of a lot of large ellipticals:

$$\log I(r) = \log I(0) - C\, r^{1/4}, \tag{47}$$

where $I(0)$ is the surface-brightness in the center and C a parameter which depends on the size of the galaxy. Because of the power law which defines it, it is sometimes referred to as the $r^{1/4}$ law. Often it is defined by expliciting the effective radius r_{e} and the effetive luminosity I_{e}, which are respectively the radius inside which half of the total luminosity is found and the surface brightness at that radius:

$$\log \frac{I(r)}{I_{\mathrm{e}}} = -k \left(\left(\frac{r}{r_{\mathrm{e}}} \right)^{1/4} - 1 \right) \tag{48}$$

where $k \simeq 3.25$ according to the original paper. Burkert (1993) by investigating a large sample of massive elliptical galaxies found that their surface

brightness profile follows the de Vaucouleurs law with deviations smaller than 5% in the range $0.1\,r_\mathrm{e} < r < 1.5\,r_\mathrm{e}$, but not so well elsewhere.
The de Vaucouleurs law works well for giant elliptical galaxies, but not so well for the smaller ones. Caon et al. (1993) showed that the surface brightness of smaller elliptical galaxies is better described by the *Sérsic law*. Proposed by Sérsic (1963), this formula replaced the $r^{1/4}$ power law by de Vaucouleurs with a more general $r^{1/n}$ power law:

$$\log \frac{I(r)}{I_\mathrm{e}} = -b_n \left(\left(\frac{r}{r_\mathrm{e}} \right)^{1/n} - 1 \right) \tag{49}$$

where n is called Sérsic index and the coefficient b_n depends on n and is defined as the solution of $2\gamma(2n, b) = \Gamma(2n)$, so that r_e contains half of the total luminosity ($\Gamma(a) = \int_0^\infty t^{a-1}e^{-t}dt$ is the gamma function and $\gamma(a, x) = \int_0^x t^{a-1}e^{-t}dt$ is the lower incomplete gamma function). An approximate solution for $0.5 < n < 10$ is given by:

$$b \simeq 2\,n - 1/3 + 0.009876(1/n) \tag{50}$$

(Prugniel & Simien 1997). Observations show that giant elliptical galaxies have a Sérsic index $n \simeq 4$ or larger, while dwarf ellipticals and the spheroids of spiral galaxies have a smaller value of n, up to $n = 1$. The Sérsic law therefore describes a much wider range of elliptical galaxies, and for this reason it has been chosen as the blueprint of the models generated by the code. In principle it is possible to directly deproject the de Vaucouleurs law or the Sérsic law to get a tridimensional density profile, but the result is not analytical or involves special functions (Baes & Gentile 2011). For this reason, when doing analytical studies or numerical simulations it is more convenient to use more simple density profiles which approximate those direct deprojections. In the rest of this chapter I will discuss the ones used in the code.

3.2 Jaffe profile

The *Jaffe profile* is a model for the mass density of elliptical galaxies proposed by Jaffe (1983). Its projection along the line of sight is close to the de Vaucouleurs law, but unlike the direct deprojection it has the advantage of being very simple, allowing to deduce analitically many of its properties. It has the following expression:

$$\rho(r) = \frac{\rho_0}{4\pi} \left(\frac{r}{r_0} \right)^{-2} \left(1 + \frac{r}{r_0} \right)^{-2} \tag{51}$$

where r_0 is the half-mass radius, which is the radius inside which half of the total mass is contained, and ρ_0 is a parameter to be determined from the desired total mass. In fact, the mass contained within radius r can easily be obtained by integration:

$$M(r) = \frac{\rho_0 r_0^3}{4\pi} \int_0^{r/r_0} \frac{4\,\pi\, z^2\, dz}{z^2(1+z)^2} = \rho_0\, {r_0}^3 \frac{r}{r_0 + r}. \tag{52}$$

In the limit $r \to \infty$ we have that the total mass is $M = M(\infty) = \rho_0\, {r_0}^3$, therefore ρ_0 can be defined as $\rho_0 = M/r_0^3$; it can also be noted that $M(r_0) = M/2$.
In the Jaffe profile the half-mass radius radius r_0 is related to the effective radius r_e by:

$$r_\mathrm{e} \simeq 0.763 r_0 \tag{53}$$

Using the Poisson equation in spherical coordinates, the gravitational potential generated by a galaxy distributed according to the Jaffe profile is:

$$\Psi(r) = \frac{GM}{r_0} \log\left(1 + \frac{r_0}{r}\right). \tag{54}$$

It is also possible to analitically calculate the distribution function for an isotropic galaxy with a single Jaffe component using Equation (38). In fact, the density can be expressed as a function of the potential as:

$$\rho(\Psi) = \rho_0 \left(e^{\frac{r_0}{2GM}\Psi} - e^{-\frac{r_0}{2GM}\Psi}\right)^4 \tag{55}$$

which has second derivative:

$$\frac{d^2\rho}{d\Psi^2} = \frac{1}{\pi G^2 M r_0} \left(e^{\frac{2r_0}{GM}\Psi} - e^{\frac{r_0}{GM}\Psi} - e^{-\frac{r_0}{GM}\Psi} + e^{-\frac{2r_0}{GM}\Psi}\right). \tag{56}$$

By replacing Equation (56) in Equation (38) we obtain the distribution function for a self-gravitating Jaffe model:

$$f(\mathcal{E}) = \frac{M}{2\pi^3 (G^2 M r_0)^{3/2}} (F_-(\sqrt{2\tilde{\mathcal{E}}}) - \sqrt{2} F_-(\sqrt{\tilde{\mathcal{E}}}) - \sqrt{2} F_+(\sqrt{\tilde{\mathcal{E}}}) + F_+(\sqrt{2\tilde{\mathcal{E}}})) \tag{57}$$

where $\tilde{\mathcal{E}} = -r_0\mathcal{E}/GM$ and $F_\pm(x) = e^{\mp x^2} \int_0^x e^{\pm x'^2} dx'$ is the Dawson integral.

3.3 Hernquist profile

The *Hernquist profile* has been derived by Hernquist (1989), as a variant of the Jaffe profile which better resembles the de Vaucouleurs law at small radii:

$$\rho(r) = \frac{M}{2\pi}\frac{a}{r}\frac{1}{(r+a)^3} \tag{58}$$

where a is a scale parameter, which we will address as the Hernquist parameter. It is related to the half-mass radius and to the effective radius as it follows:

$$r_{1/2} = (1+\sqrt{2})a \simeq 1.33 r_{\rm e}. \tag{59}$$

The cumulative mass distribution (i.e., the mass contained inside the radius r) is:

$$M(r) = M\frac{r^2}{(r+a)^2}. \tag{60}$$

Using the Poisson equation, the gravitational potential generated by this model has the very simple form:

$$\Psi(r) = -\frac{GM}{r+a}. \tag{61}$$

Although originally intended for describing the luminous part of elliptical galaxies, the Hernquist profile has also been often used to describe dark matter halos (Ciotti 1996) because of its simplicity and its mathematical properties, for instance the fact that its integral is finite; a property that the NFW profile (Navarro et al. 1996), which is the most widely used profile to fit dark matter halos, does not satisfy.

3.4 Prugniel-Simien profile

This density profile, obtained Prugniel & Simien (1997), is actually a generalization to the Sérsic law of an older profile which closely approximated the deprojection of the de Vaucouleurs law (Mellier & Mathez 1987), without being too complex to handle. It has the following expression:

$$\rho(r) = \rho_0 \left({b_n}^n \frac{r}{r_{\rm e}} \right)^{-p} \exp\left(-b_n \left(\frac{r}{r_{\rm e}} \right)^{1/n} \right) \tag{62}$$

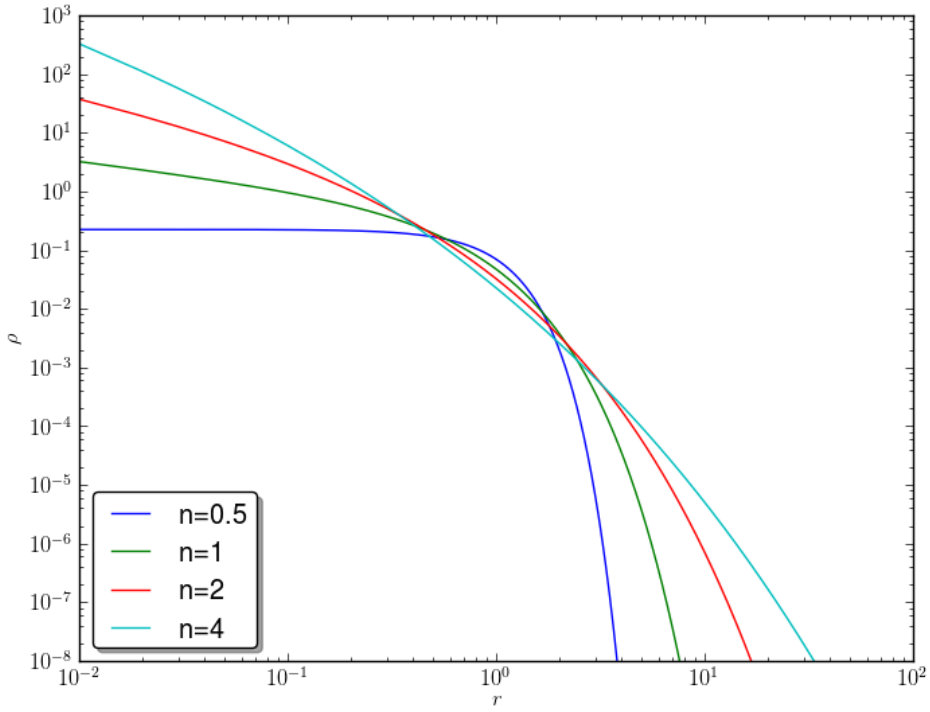

Figure 2: Plot of the Prugniel-Simien (Sérsic) mass density profile for different values of the Sérsic index ($n = 0.5, 1, 2, 4$), with the same total mass ($M = 1$) and effective radius ($r_{\rm e} = 1$).

where n and b_n are the same parameters of the Sérsic law and p is a parameter that depends on n and has to be obtained by fitting the direct deprojection of the Sérsic law. A good approximation (Terzić & Graham 2005) for $0.6 < n < 10$ is

$$p \simeq 1.0 - 0.6097(1/n) + 0.05463(1/n)^2. \tag{63}$$

For simplicity we can define

$$x = b^n \frac{r}{r_{\rm e}} \tag{64}$$

so that the *Prugniel-Simien profile* has the following expression:

$$\rho(r) = \rho_0 x^{-p} \exp\left(-x^{1/n}\right). \tag{65}$$

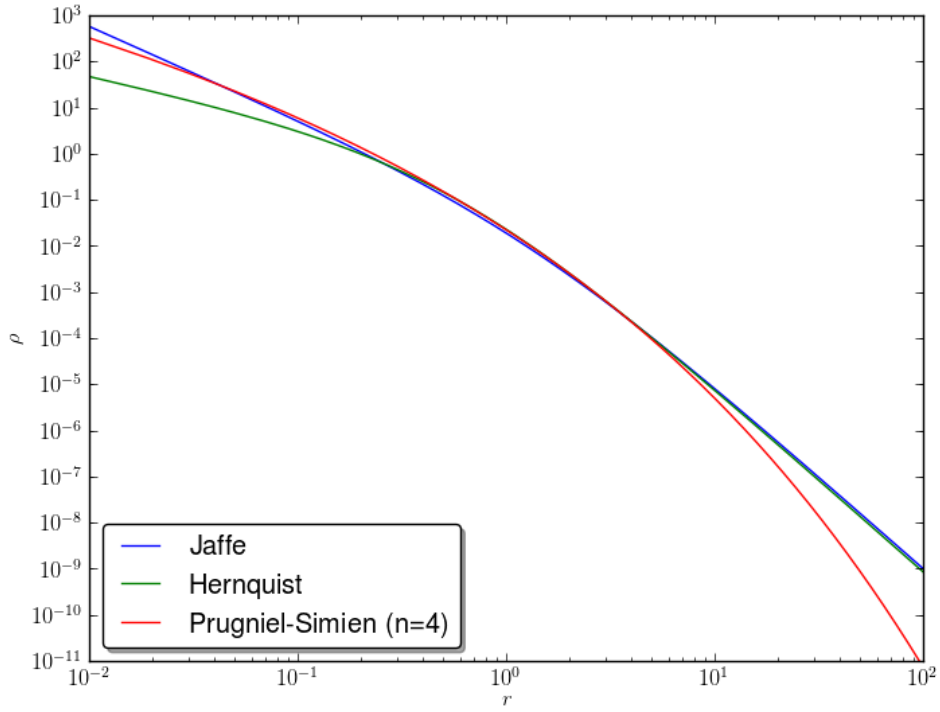

Figure 3: Plot of the Jaffe (blue line), Hernquist (green line) and Prugniel-Simien ($n = 4$; red line) density profiles with the same total mass ($M = 1$) and effective radius ($r_{\rm e} = 1$).

The parameter ρ_0 is normalized so that the total mass is M:

$$\rho_0 = \frac{M}{4\,\pi\,n\,\Gamma(n(3-p))}\left(\frac{b^n}{r_{\rm e}}\right)^3. \tag{66}$$

In this case the relation between the effective radius $r_{\rm e}$ and the half-mass radius $r_{1/2}$ also depends on n:

$$r_{1/2} \simeq (1.356 - 0.0293(1/n) + 0.0023(1/n)^2) r_{\rm e}. \tag{67}$$

The cumulative mass distribution is:

$$M(r) = M\frac{\gamma(n(3-p), x^{1/n})}{\Gamma(n(3-p))} \tag{68}$$

and the potential generated by this density profile through the Poisson equation is:

$$\Psi(r) = 4\,\pi\,G\,n\,\rho_0\left(\frac{b^n}{r_{\rm e}}\right)^{-2}\cdot \\ \cdot\left(\frac{1}{x}\gamma\left(n(3-p),x^{1/n}\right)+\Gamma\left(n(2-p),(x^{1/n})\right)\right) \quad (69)$$

where $\gamma(a,x)=\int_0^x t^{a-1}e^{-t}dt$ and $\Gamma(a,x)=\int_x^\infty t^{a-1}e^{-t}dt$ are the lower and upper incomplete Gamma functions, respectively.
Once projected, this density profile approximates almost perfectly the Sérsic law for every n. The accuracy and the versatilness of the Prugniel-Simien profile, are the reason why such a mass density profile has been chosen for building the luminous component of the models. In Figure 2 several Prugniel-Simien profiles with the same mass and effective radius but different values of n are plotted, showing that profiles with higher n have a higher density in the central and outer regions, while profiles with lower n are more concentrated at $r\sim r_{\rm e}$. In profiles with $n<0.5$ the density decreases towards the center, giving rise to a ring-like galaxy. In the inner parts the profiles tend to follow $\rho\propto r^{-p}$.
Figure 3 shows a comparison between the Jaffe, Hernquist and Prugniel-Simien (with $n=4$) profiles. The Prugniel-Simien profile with $n=4$ closely reproduces the de Vaucouleurs law. Relatively to it the Jaffe profile is steeper near the center and more shallow in the outer parts, while the Hernquist profile is more shallow in both inner and outer regions.

4 Numerical methods used in the code

This chapter describes the numerical methods that allow the code to create stable and accurate models with a finite number of particles. For each particle, the code first assigns a pseudo-random position so that the overall density follows the selected mass density profile (Section 4.1). Then it generates a pseudo-random velocity according to the distribution function $f(Q)$ associated with that density profile, so that the shape and properties of the galaxy remain stable (Section 4.2). The distribution function itself needs to be evaluated numerically. To this aim the Gauss-Chebyshev quadrature was adopted, since it is computationally very fast without sacrificing accuracy (Section 4.3).

4.1 Inversion method for generating positions

There are two main methods for generating random numbers according to a given distribution (see Devroye 1986): the *inversion method* and the *rejection method*, and they are both used in the code, for the positions and for the velocities respectively.
The inversion method is also known as inverse transform method or Smirnov transform. It is based on the fact that if X is a pseudo-random variable with cumulative distribution $F(x)$, then $Y = F(X)$ must be a uniform distribution between 0 and 1. Therefore, inverting this equation we obtain that if Y is a random number between 0 and 1 then:

$$X = F^{-1}(Y) \tag{70}$$

is a pseudo-random variable with cumulative distribution $F(x)$.
In the code this is used to generate the radius r of the particles according to the given mass density profile. We need r to be distributed according to the distribution $f(r)dr = 4\pi r^2 \rho(r) dr$. If we define $u = 1/r$, the cumulative distribution function associated with this variable has to be:

$$F(u) = \frac{\frac{d\Psi}{du}(u)}{\left(\frac{d\Psi}{du}\right)_{u\to\infty}}. \tag{71}$$

This in fact is a monotone increasing function that goes from 0 to 1 and it has derivative:

$$f(u) = \frac{dF}{du}(u) = C\,\frac{d^2\Psi}{du^2}(u) \tag{72}$$

where we defined $C = \left(\frac{d\Psi}{du}\right)_{u\to\infty}$. Changing variable from u to r it is:

$$f(u)\,du = C\,\frac{\partial r}{\partial u}\,\frac{\partial}{\partial r}\left(\frac{\partial r}{\partial u}\,\frac{\partial \Psi}{\partial r}\right)\,\frac{\partial u}{\partial r}\,dr = -C\,\frac{\partial}{\partial r}\,\left(r^2\frac{\partial \Psi}{\partial r}\right)dr = \\ = -C\,r^2\,\nabla^2\Psi\,dr \quad (73)$$

where we used the polar expression of the Laplacian operator ∇^2. Using now the Poisson equation we obtain:

$$f(u)\,du = -4\,\pi\,G\,C\,r^2\,\rho(r)\,dr = -G\,C\,f(r)\,dr. \quad (74)$$

Therefore, by distributing $u = 1/r$ according to the cumulative distribution in Equation (71) we automatically distribute r according to the density profile. Applying the inversion method then, the variable u has to be generated by $u = F^{-1}(Y)$, where Y is a random variable distributed between 0 and 1. In the code the inversion is done by numerically solving for u the following equation:

$$\left(\frac{d\Psi}{du}(u)\right) = Y\,\left(\frac{d\Psi}{du}\right)_{u\to\infty}. \quad (75)$$

Once the distance from the center is generated with this method, the angles that complete the determination of the position of the particle are generated purely randomly (because the models are spherically simmetric).

4.2 Rejection method for generating velocities

The inversion method is very elegant, but it requires that the distribution function is analytical. This is not the case for the velocities of our particles. Since the distribution function is obtained by numerical integration we have to use another method. The rejection method, also known as rejection sampling or accept-reject method, is basically a Montecarlo method for distributing a random variable X according to a distribution $f(x)$. It consists in generating random values of X and then accepting or rejecting them depending on the comparison between the distribution function in X and a random value that can assume any value between 0 and the maximum of the function. If the random value is smaller than the value of the function, then X is accepted, otherwise it is rejected. If Y is a random number between 0 and 1, it results:

$$\begin{cases} \text{if } Y \cdot f_{\max} \leq f(X) \;\Rightarrow\; X \text{ is accepted} \\ \text{if } Y \cdot f_{\max} > f(X) \;\Rightarrow\; X \text{ is rejected} \end{cases} \quad (76)$$

. Where the distribution function $f(x)$ is larger it is more probable for the values of X to be accepted, and if the number of samples is large enough then X will be distributed exactly as in $f(x)$.
In the code the radial velocity v_r and the tangential velocity v_t are first randomly generated within the available range at their distance from the center. In fact the condition for a particle to be in a bound orbit is that its kinetic energy is smaller than its potential energy:

$$0 < \frac{{v_r}^2 + {v_t}^2}{2} < \Psi(r). \tag{77}$$

Then the code calculates the value of Q (Equation (41)) associated with these velocities, and it applies the rejection method with the distribution function $f(Q)$ to decide whether to accept it or not. In principle one might pick a value of $f_{\max}$ that is larger than all possible values of $f(Q)$, at all radii, but it is computationally more efficient to pick the smallest value that is larger than $f(Q)$ for any Q in the range available at that radius (Equation (77)). The code therefore divides the range of radii into a number of bins and calculates the value $f_{\max}$ for each of them. If the value of Q is not accepted a new pair of radial and tangential velocities is generated and the process starts over, until a value is accepted.

4.3 Gauss-Chebyshev quadrature for calculating the distribution function

The distribution function $f(Q)$ is calculated from the Osipkov-Merritt formula (Equation (46)), but the integral in that equation has to be calculated numerically. Since this integral has to be calculated several times for each particle, it is important to have an integration algorithm that is not too computationally expensive. On the other hand, the integrand is very steep near the center, therefore the algorithm also has to be able to handle this quasi-divergence. The integration method chosen in the code is the Gaussian quadrature with Chebyshev polinomials (see Press et al. 1986, Chapter 4.5).

A Gaussian quadrature estimates an integral of the type $\int_a^b W(x)f(x)dx$ as a weighted sum of values of the function f:

$$\int_a^b W(x)f(x)dx \simeq \sum_{j=1}^{N} w_j f(x_j) \tag{78}$$

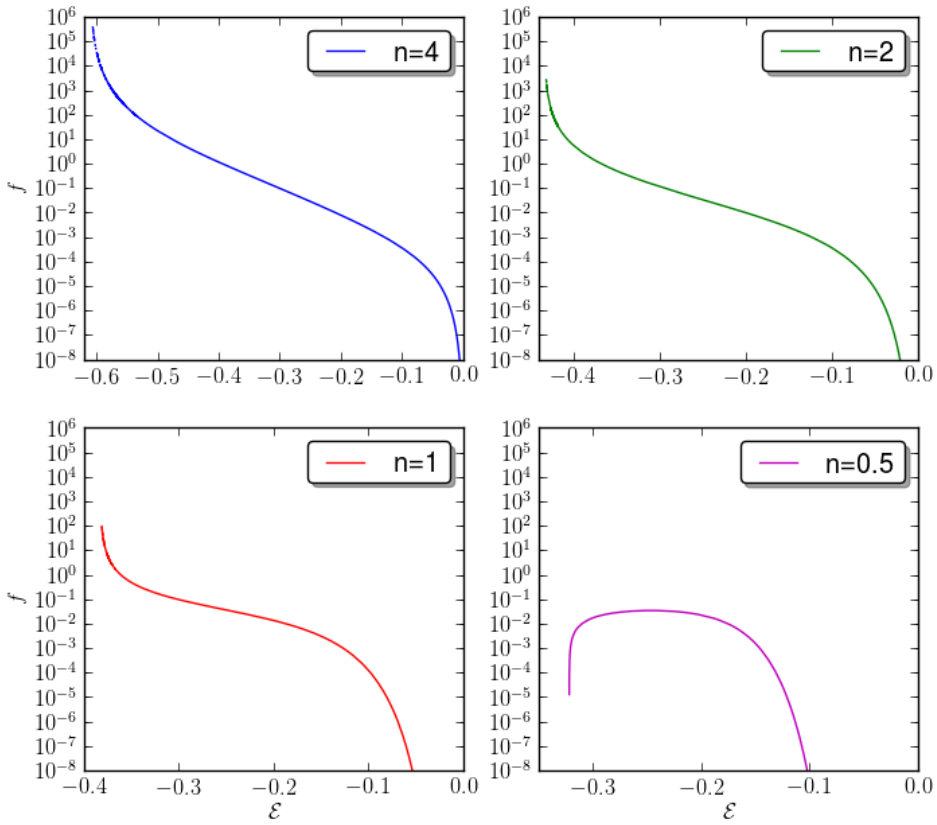

Figure 4: Comparison between the distribution functions of 4 isotropic Prugniel-Simien models with the same mass and effective radius but different Sérsic indices ($n = 0.5, 1, 2, 4$). In all the models the luminous component has mass $M = 0.1$ and half-mass radius $r_{1/2} = 1$, while the dark matter component has mass $M = 0.5$ and half-mass radius $r_{1/2} = 5$.

where the weighting function $W(x)$, weights w_j, and values x_j in which the integrand is evaluated are all related and determined by the choice of a set of polynomials. In fact, the function $W(x)$ is the one that makes the polynomials orthogonal over the scalar product defined as:

$$\langle f|g\rangle \equiv \int_a^b W(x)f(x)g(x)dx \tag{79}$$

while the values x_j are the roots of the polynomial of order N, where N is the desired number of evaluations (parameter `ncheb` in the code). Choosing the Chebyshev polinomials, which are defined as $T_n \equiv \cos(n \cos^{-1} x)$, we have

$$W(x) = \frac{1}{\sqrt{1-x^2}},\ x_j = \cos\left(\frac{\pi(j-\frac{1}{2})}{N}\right),\ w_j = \frac{\pi}{N}. \tag{80}$$

and the integration range is $-1 < x < 1$. However, in our case we need to integrate from 0 to 1, therefore the values x_j and the weights w_j have been changed into:

$$x_j = \cos\left(\frac{\pi(j-\frac{1}{2})}{2N}\right),\ w_j = \frac{\pi}{2N}. \tag{81}$$

Putting all together, the formula used to calculate the integral is:

$$\int_0^1 \frac{f(x)}{\sqrt{1-x^2}}\,dx \simeq \frac{\pi}{2N}\sum_{j=1}^{N} f(x_j). \tag{82}$$

To put Equation (46) in this format we change the integration variable to $u = 1/r$, which yields $d\Psi = \frac{d\Psi}{du}du$:

$$f(Q) = \frac{1}{2\sqrt{2}\pi^2}\int_0^{\Psi^{-1}(Q)} \frac{d^2\rho_Q}{d\Psi^2}(u)\,\frac{d\Psi}{du}(u)\frac{1}{\sqrt{\Psi(u)-Q}}du. \tag{83}$$

Changing again variable to $z = u/\Psi^{-1}(Q)$ we then obtain:

$$f(Q) = \frac{\Psi^{-1}(Q)}{2\sqrt{2}\pi^2}\int_0^1 \frac{d^2\rho_Q}{d\Psi^2}\,\frac{d\Psi}{du}(z\Psi^{-1}(Q))\sqrt{\frac{1-z^2}{\Psi(z\Psi^{-1}(Q))-Q}}\frac{dz}{\sqrt{1-z^2}} \tag{84}$$

It is now possible to apply the Gauss-Chebyshev integration formula (Equation (82)), to get the formula used in the code:

$$f(Q) = \frac{\Psi^{-1}(Q)}{4\sqrt{2}N\pi}\sum_{j=1}^{N} \frac{d^2\rho_Q}{d\Psi^2}\,\frac{d\Psi}{du}(z_j\Psi^{-1}(Q))\sqrt{\frac{1-{z_j}^2}{\Psi(z_j\Psi^{-1}(Q))-Q}} \tag{85}$$

where z_j is the x_j given by Equation (81). The second derivative of ρ_Q as a function of u can be calculated from its definition (Equation (45)) obtaining:

$$\frac{d^2\rho_Q}{d\Psi^2}(u) = \frac{1}{\Psi'^3}[(1-\frac{1}{(r_a u)^2})(\rho''\,\Psi' - \rho'\,\Psi'') - \\ - \frac{1}{{r_a}^2 u^3}(2\rho\,\Psi'' - 4\,\rho'\,\Psi' + \frac{6\,\rho\,\Psi'}{u})] \tag{86}$$

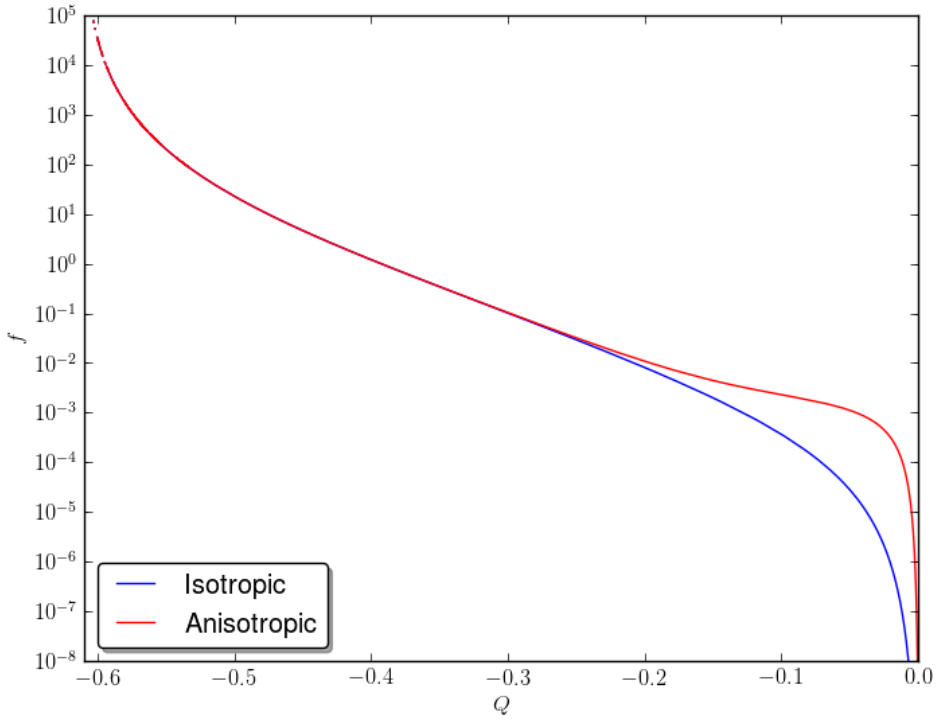

Figure 5: Distribution functions of different two-component models calculated with the Osipkov-Merritt formula and applying the Gauss-Chebyshev method for the integration. In both models the luminous component follows the Prugniel-Simien profile with Sérsic index $n = 4$, mass $M = 0.1$ and half-mass radius $r_{1/2} = 1$, while the dark matter component has mass $M = 0.5$ and half-mass radius $r_{1/2} = 5$. In the anisotropic case (red line) the anisotropy radius is set to $r_\mathrm{a} = 1 = r_{1/2}$.

where $'$ identifies the derivative with respect to u. In the isotropic case it reduces to:

$$\frac{d^2\rho}{d\Psi^2}(u) = \frac{\rho''\Psi' - \rho'\Psi''}{\Psi'^3}. \tag{87}$$

The distribution functions of several Sérsic models with different Sérsic indices is shown in Figure 4, showing that larger indices and thus larger cetral densities make the distributions reach larger energies. Figure 5 shows the comparison between the distribution functions of an isotropic and an anisotropic model.

5 Features of the code and properties of the generated models

In this chapter the features and input parameters of the code are presented (Section 5.1), and the models generated with it are analyzed. In Section 5.2 is discussed the accuracy of the generated models and in Section 5.3 their stability over time.

5.1 Usage of the code

As already stated, the code generates stable anisotropic models of spherical galaxies with two components: a dark matter component with mass density following the Hernquist profile and a luminous matter component with mass density following either the Jaffe or the Prugniel-Simien profile, with Sérsic index chosen by the user. The user can also select the size and mass of both the luminous and dark components, the anisotropy radius and the number of particles. All these options can be selected in the `num.par` file, and are listed in Table 1.
The models are generated in the `.xvp` format, a direct access binary format for N-body data developed by Marc Balcells[2], which for each particle contains position, velocity, mass, and gravitational potential in its location, and it allows to group the particles in different groups. Simple software is available to convert `.xvp` files into the `.ggd` format used for instance in the N-body software Gadget 2 (Springel 2005). The `.ggd` format contains the same information of the `.xvp` format except the gravitational potential. Moreover, it distinguishes its groups of particles in different types (disk, bulge, gas,...) that can be treated differently by Gadget 2.

5.2 Accuracy and properties of the models

In this section we will take a look at how well the models satisfy the properties selected by the user. The units used in all the figures are the internal units of the model with $G = 1$, which can easily be converted to any desired set of units, as long as $G = 1$ remains satisfied (for instance one might choose

[2]Additional information on the `.xvp` format can be found at `http://bima.astro.umd.edu/nemo/man_html/xvp.5.html`

Parameter	Description
`denstype`	Type of (luminous) mass density profile: 0 = Prugniel-Simien, 1 = Jaffe
`nsersic`	Sérsic index of the luminous component (ignored if `denstype`=1)
`gravc`	Gravitational constant, G
`mhalo`	Mass of the dark (Hernquist) component
`rhalo`	Half-mass radius of the dark (Hernquist) component
`mbulge`	Mass of the luminous (Prugniel-Simien/Jaffe) component
`rbulge`	Half-mass radius of the luminous (Prugniel-Simien/Jaffe) component
`ra1, ra2`	Anisotropy radius of the luminous and dark components (use high values for isotropic model)
`umin`	1/(Maximum radius of the model)
`umax`	1/(Minimum radius of the model)
`ncheb`	Number of terms in Gauss-Chebyshev integration formula
`eps`	Arbitrary small number to set the accuracy of the code
`nn`	Number of particles of the luminous component
`np`	Total number of particles (of both components)
`iseed`	Seed for the random number generator
`nbins`	Number of bins for estimating the maximum value of the PDF

Table 1: Description of the parameters in the `num.par` file.

[L]=0.8 kpc, [M]=$10^{12}\,M_\odot$, [T]=0.34 Myr, [V] = $2318.14 km\,s^{-1}$). Figure 6 shows the mass density and velocity dispersion profiles of a model generated by a specific set of parameters. The mass density profile of both the luminous and dark components are compared with the analytical mass density profiles following Prugniel-Simien and Hernquist laws. The match is very good. The surface-brightness of the model is also very similar to the analytical prediction. Figure 7 shows the surface brightness of the model fitted with a Sérsic law with the Sérsic index, effective radius and central brightness as free parameters, and the residuals of the fit. The parameters obtained by the fit are close to the input ones. We found $n = 4.20$ instead of $n = 4.13$, and $r_{\rm e} = 1.332$ instead of $r_{\rm e} = 1.330 (= 0.784\, r_{1/2})$. The χ^2 value of the fit is 67.73, giving a reduced ${\chi_\nu}^2 = 1.69$. With smaller Sérsic indices the data is

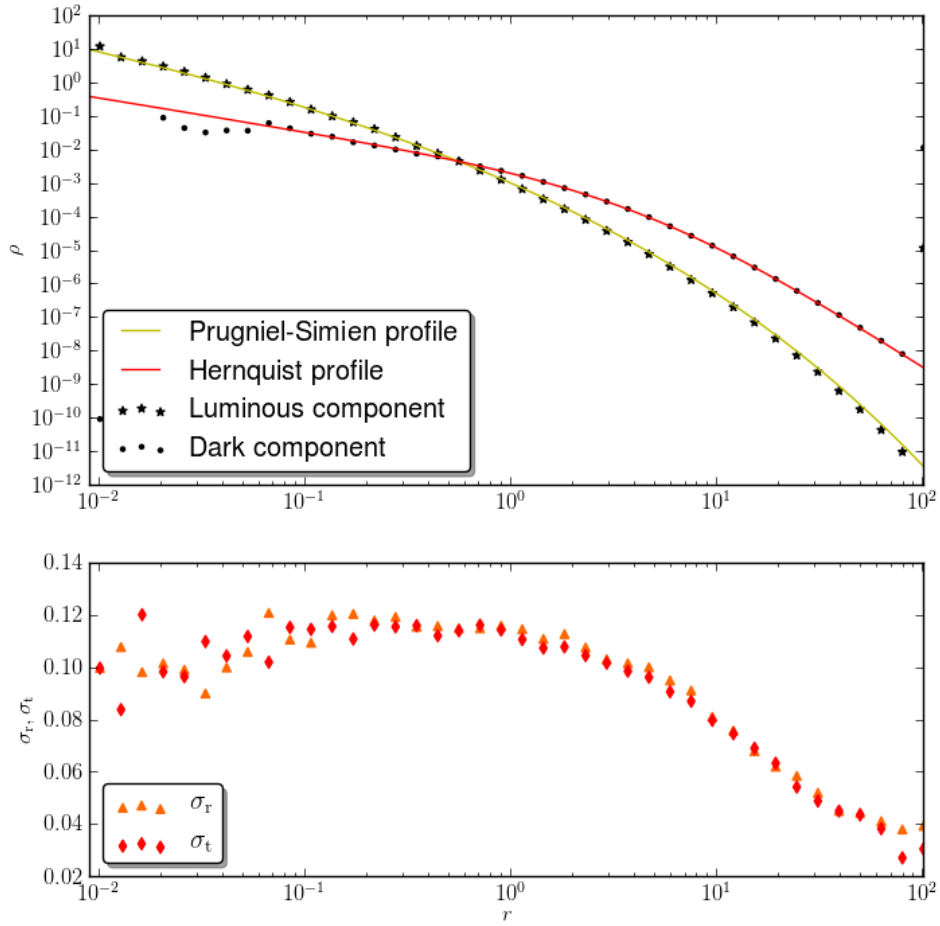

Figure 6: Example of density and velocity dispersion profiles of a model generated by the code. The upper plot shows the mass density profile of both the luminous and dark components of the galaxy, comparing them with the Prugniel-Simien and Hernquist density profiles of the same mass, effective radius and Sérsic index. The lower plot shows the radial and tangential velocity dispersions of the luminous component. The adopted model is isotropic and has parameters `nsersic`=4.13, `mhalo`=0.52, `rhalo`=11.4, `mbulge`=0.052, `rbulge`=1.696, `nn`=50000, and `np`=250000 (see Table 1).

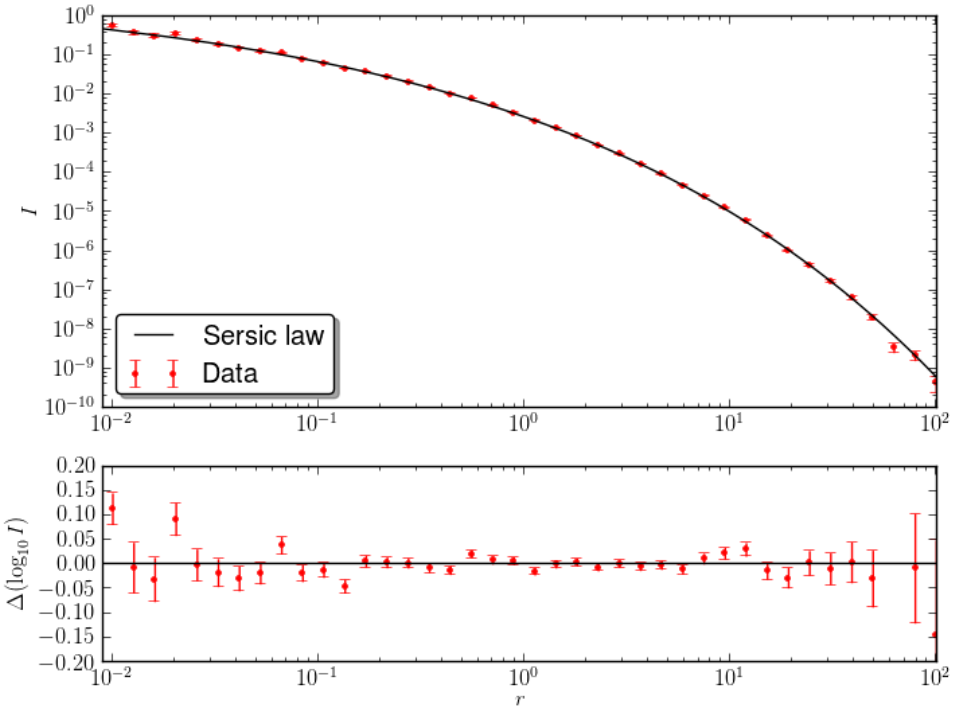

Figure 7: Fit with a Sérsic law of the surface-brightness radial profile of a model generated by the code. The model is isotropic and was generated with input parameters `nsersic`=4.13, `mhalo`=0.52, `rhalo`=11.4, `mbulge`=0.052, `rbulge`=1.696, `nn`=50000 and `np`=250000. The result of the fit is $n_{\rm fit} \simeq 4.2$, with $\chi^2_\nu = 1.69$.

closer to the Sérsic law, getting to ${\chi_\nu}^2 = 0.46$ in the models with $n = 1$. The complete data set is given in Table 4.

5.2.1 Shape of the line-of-sight velocity dispersion

The shape of the line-of-sight velocity dispersion $\sigma_{\rm los}$ of the models is determined by several properties of the galaxy, which can be modified in the `num.par` file. Figures 8 and 9 show how the mass and size (half-mass radius) of the dark matter halo influence the velocity dispersion of the luminous component respectively. A more massive halo makes the velocity dispersion higher around the half-mass radius, while a smaller halo in size increases

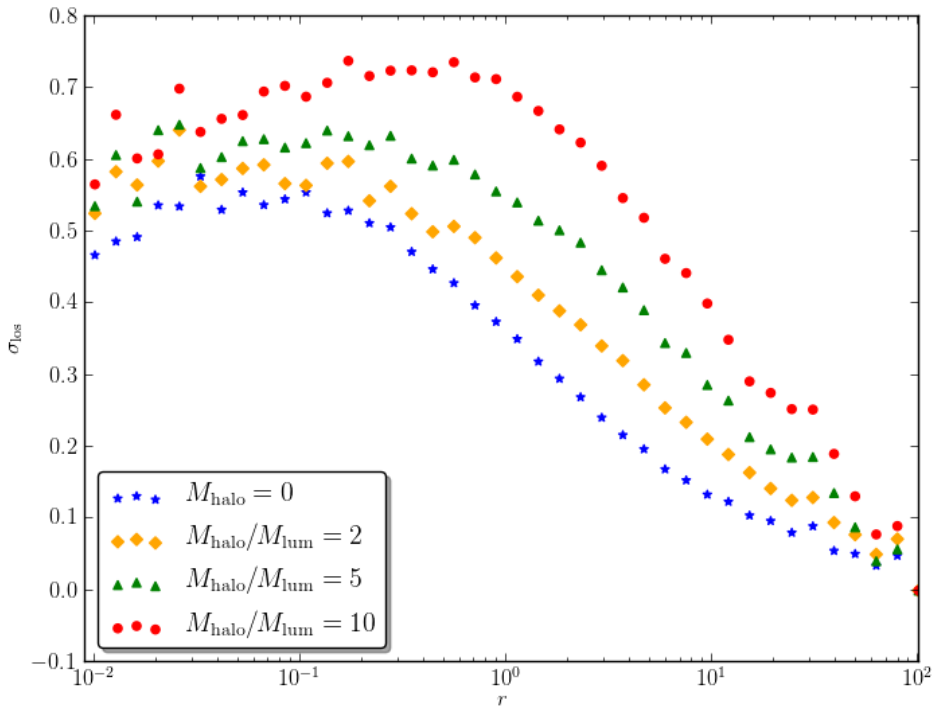

Figure 8: Comparison of the velocity dispersion of models in which the dark matter halo has different masses. In all the models the half-mass radius of the dark halo is $r_{1/2,\rm halo} = 5$, while the luminous component is isotropic and has mass $M_{\rm lum} = 1$, half-mass radius $r_{1/2,\rm lum} = 1$ and Sérsic index $n = 4$.

the velocity dispersion near the center. The velocity dispersion also depends on the anisotropy of the models, and Figure 10 compares a purely isotropic model with a model in which the anisotropy radius of the luminous component is $r_{\rm a} = 1$.

5.3 Stability of the models

The models are generated with velocities assigned by the code so that the whole system remains stable, meaning that its macroscopic properties (e.g., the effective radius and Sérsic index) remain constant over time. Here we will take a look at how well these properties are conserved by simulating the

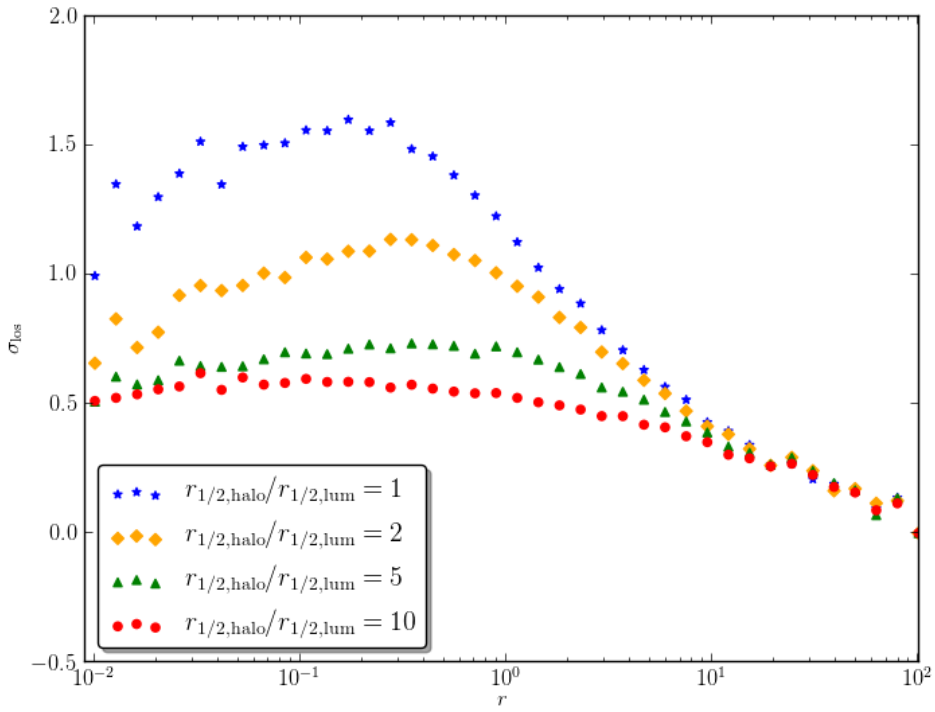

Figure 9: Comparison of the velocity dispersion of models in which the dark matter halo has different sizes. In all the models the mass of the dark halo is $M_{\rm halo} = 10$, while the luminous component is isotropic and has mass $M_{\rm lum} = 1$, half-mass radius $r_{1/2,\rm lum} = 1$ and Sérsic index $n = 4$.

time evolution of the models in an isolated state. The time evolution has been carried out by the software Gadget 2 (Springel 2005) after converting the models to the `.ggd` format.

5.3.1 Size

Table 2 compares the half-mass radius of the luminous matter selected in the `num.par` file with the one of the actual model generated by the code at time 0 and after the model has been relaxed (evolved in isolation). A few different cases are taken into account. In each case the galaxy has the same mass, size, and number of particles (`mbulge`=0.052, `rbulge`=1.696,

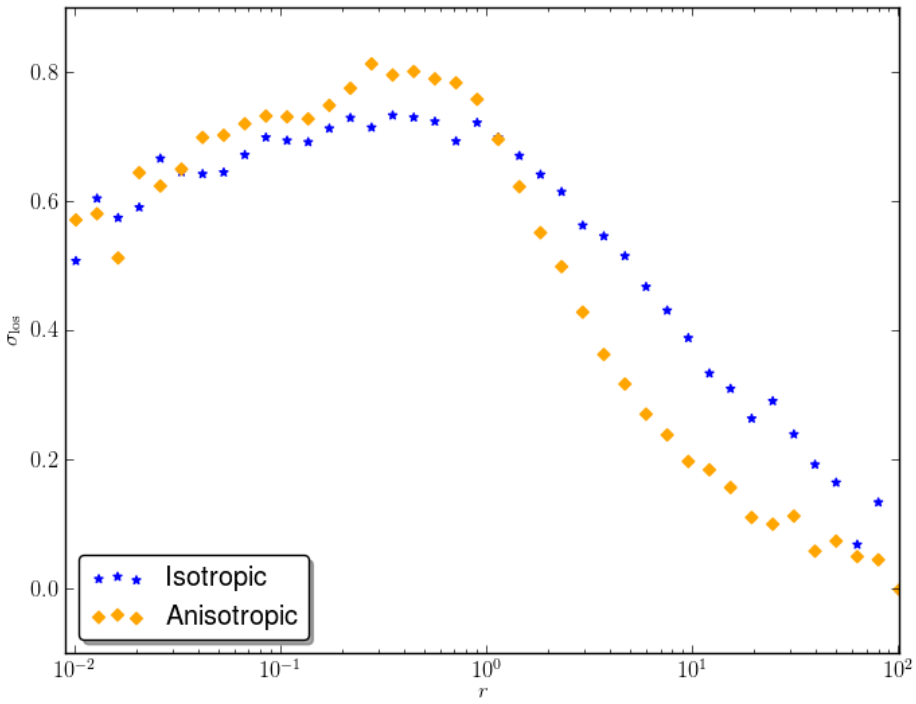

Figure 10: Comparison of the velocity dispersion of an isotropic and an anisotropic model, with anisotropy radius $r_{\rm a} = 1$. In both models the luminous component has mass $M_{\rm lum} = 1$, half-mass radius $r_{1/2,\rm lum} = 1$ and Sérsic index $n = 4$, while the dark component has mass $M_{halo} = 10$ and half-mass radius $r_{1/2,\rm halo} = 5$.

`mhalo`=0.52,`rhalo`=11.4, `nn`=50000 and `np`=250000) but different Sérsic index.

We can have a better look at the stability of the models by plotting the radii containing 1%, 2%, ..., 90% of the mass of the galaxy as a function of time. This is shown in Figure 11 for a model with $n = 4$. The figure shows that the models are mostly stable, and the half-mass radius is almost perfectly conserved. In the graph time is expressed in units of *crossing time*. The crossing time is a characteristic timescale of the evolution of a gravitational system and is defined as:

$$t_{\rm cross} = \sqrt{\frac{{r_{1/2}}^3}{G\,M}}. \tag{88}$$

Input value $r_{1/2,\mathrm{input}}$	Value at time 0 $r_{1/2}(0)$	Value after relaxation $r_{1/2}(t_{\mathrm{rel}})$	Sersic Index n
1.70	1.55	1.57	4
1.70	1.72	1.64	2
1.70	1.71	1.62	1

Table 2: Half-mass radius of the luminous matter component.

Input value $r_{1/2,\mathrm{input}}$	Value at time 0 $r_{1/2}(0)$	Value after relaxation $r_{1/2}(t_{\mathrm{rel}})$	Maximum radius $r_{\max}$ (= 1/`umin`)
11.4	10.9	10.6	500
11.4	9.7	9.0	100
22.94	17.2	14.6	100

Table 3: Half mass radius of the dark matter component.

In the $n = 4$ case the radius including 1% of the mass expands of about 25%, but this is most likely due to the limited resolution of the time evolution software, and not to how the velocities are assigned by the code. In fact the total energy of the system varies of a factor 0.1% during the time evolution, whereas in the $n = 1$ case this problem does not arise and the total energy varies of 0.05%. This problem also does not affect the dark matter component, whose central part is perfectly stable as shown in Figure 12. It might instead be noted that the half-mass radius tends to shrink a little over time, and that the initial value is also smaller than the input one. This happens because the maximum radius allowed for the particles (determined by parameter `umin`) is relatively too small (`umin` too big), forcing the particles that would have been beyond the maximum radius to stay inside it and thus making the galaxy more concentrated and the half-mass radius smaller. This also makes the gravity stronger than it would be, causing the further contraction when the model evolves. Table 3 compares the shrinking of the half-mass radius for three models, showing that it depends on the size and maximum radius of the dark matter halo.

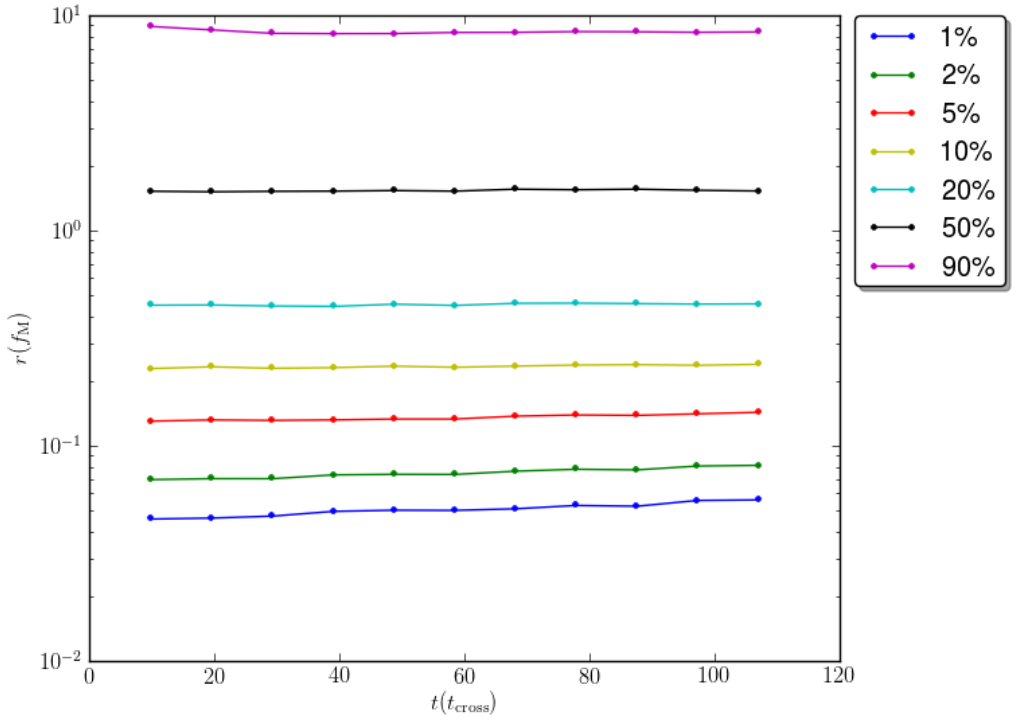

Figure 11: Time evolution of the radii including 1, 2, ..., 90% of the mass of the *luminous* component of an isotropic model with $n = 4$, mass $M_{\rm lum} = 0.052$ and half-mass radius $r_{1/2,\rm lum} = 1.696$ (input value). The time is given in units of crossing time.

5.3.2 Surface brightness and velocity dispersion

As shown in Figure 7, the surface brightness of the models is in good agreement with the Sérsic law when they are first generated. After relaxation the models seem to deviate from the Sérsic law in the inner region as we see in Figure 13, in which the same galaxy of Figure 7 has been fitted after some time evolution (about 150 crossing times). The best fit value of the Sérsic index of the surface brightness profile is $n = 3.93$, with $\chi^2 = 282.44$, which gives $\chi^2_\nu = 7.06$. Looking at the fit, it appears that this deviation is related with the expansion of the very center of the galaxy as previously observed; some particles in the center escape to the outer parts changing the shape of

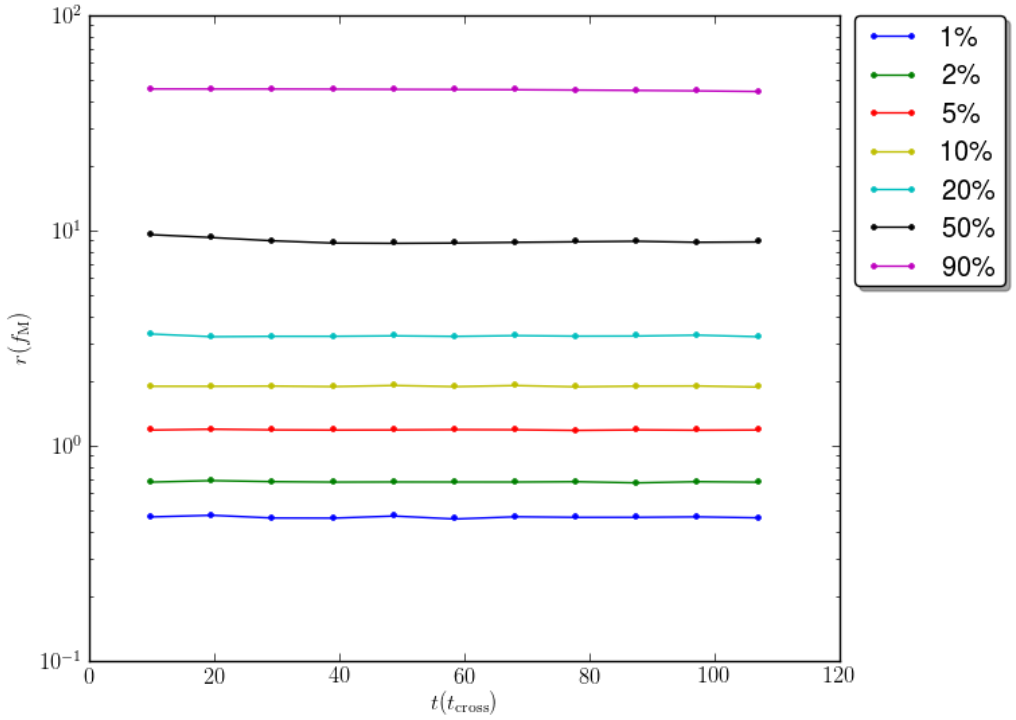

Figure 12: Plot of the time evolution of the radii inside which lies 1, 2 , ..., 90% of the mass of the *dark* component of an isotropic model. The dark halo has mass $M_{\rm dark} = 0.52$ and half-mass radius $r_{1/2,\rm dark} = 11.4$ (input values). The cutoff of the model after at radius $r_{\rm cut} = 500$. Time is given in units of crossing times (of the luminous matter).

the surface brightness profile. In fact, this effect is also much more prominent when the Sérsic index is larger. Table 4 shows the evolution of the Sérsic index in different cases.

The velocity dispersion profile is also conserved over time. Figure 14 shows the radial and tangential velocity dispersion of the same model of Figure 6, before and after relaxation. The velocity dispersions seem to get lower near the center and higher at middle ranges, which is probably related to the small expansion of the center of the galaxy caused by the evolution. The radial and tangential velocity dispersions changed in the same way, therefore the isotropy is preserved during relaxation.

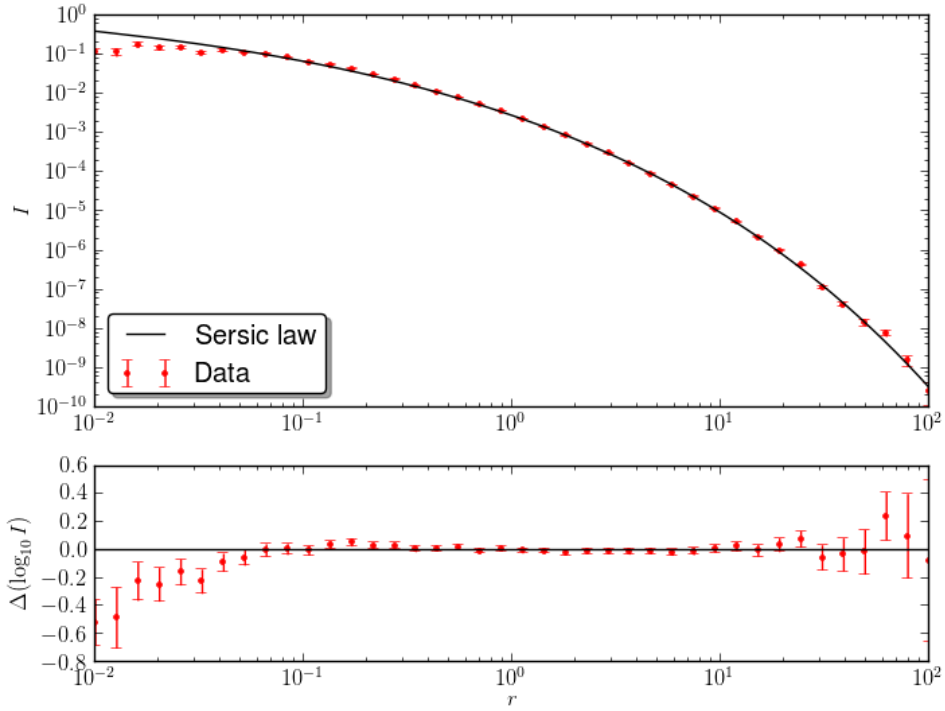

Figure 13: Sérsic law fitting of the surface brightness radial profile of a $n = 4$ model at the relaxation time. The model is the same of Figure 7, but after letting it evolve in isolation for ~ 100 dynamical times. The result of the fit is $n = 3.93$ with $\chi^2_\nu = 7.06$. The input value of the Sérsic index is $n = 4.13$, and the fitted value before relaxation $n = 4.20$.

Input value	Value at time 0		Value after relaxation	
$n_{\rm input}$	$n(0)$	$\chi^2_\nu(0)$	$n(t_{\rm rel})$	$\chi^2_\nu(t_{\rm rel})$
4.13	4.20	1.69	3.93	7.06
2.06	2.13	1.36	2.05	1.21
1.02	1.06	0.46	1.06	0.69

Table 4: Evolution of the Sérsic index.

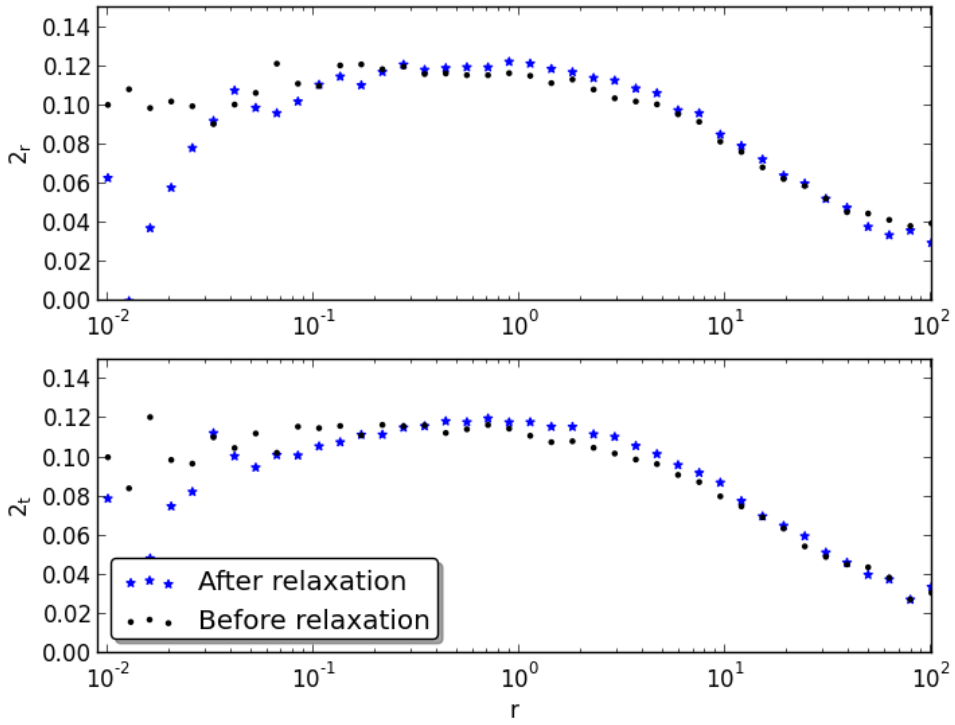

Figure 14: Radial and tangential velocity dispersion of an isotropic model with Sérsic index $n = 4$ before and after relaxation.

6 Galaxy growth through minor mergers

In this chapter an application of the code and its models is discussed. Section 6.1 presents the physical problem and the research already done on the subject, while Section 6.2 discusses the characteristics of the models and of the simulations used in the experiment. In Section 6.3 the results are shown and discussed.

6.1 Introduction

In the last years various observations have shown that the most massive elliptical galaxies at redshift $z \sim 1.5 - 2.5$ were much more compact than the ones of today (Daddi et al. 2005; Trujillo et al. 2006, 2007; van Dokkum et al. 2008; Buitrago et al. 2008). These galaxies had a mass of $M \sim 10^{12}\mathrm{M}_{\odot}$ with an effective radius of $r_{\mathrm{e}} \sim 1\,\mathrm{kpc}$, while today's galaxies of that mass have an effective radius in the order of 5 kpc. This means that the overall density of high redshift ellipticals was more than 50 times higher. Various explanations have been proposed to dismiss these observations as an observational error, such as a strong morphological K-correction or the presence of an active galactic nucleus (Daddi et al. 2005), but later observations (Trujillo et al. 2006) disproved these alternative explanations, and the existence of these compact galaxies is now well enstablished. It has also been shown that galaxies of this type do not exist in the local universe (Bernardi et al. 2006; Trujillo et al. 2009; Ferré-Mateu et al. 2012). This suggests that between $z = 2.5$ and $z = 0$ these compact ellipticals have probably evolved into the giant elliptical galaxies we see today, which is an evidence against the scenario in which early-type elliptical galaxies would have been fully assembled since $z > 1$.
The mechanism which caused this growth in size is not clear, but recently there has been a growing support for the hypothesis that the size growth of galaxies is dominated by major or minor *dry mergers*, in both low and high redshifts (van Dokkum et al. 2010; Trujillo et al. 2011; Cooper et al. 2012). Dry mergers are mergers in which the content of gas of the interacting galaxies is negligible in the dynamics of the merger itself. This hypothesis is however still controversial, as other studies have argued that a pure dry merger scenario is not completely consistent with the observations and that additional physical processes are needed especially at high redshift (Nipoti et al. 2009; Cimatti et al. 2012; Newman et al. 2012).

Because of this controversy it is interesting to understand whether dry mergers can make the compact ellipticals grow into the elliptical galaxies of the local universe. Tapia et al. (2013) tested this hypothesis by simulating various merger trees (series of successive mergers). They considered 8 merger trees that took place in the cosmological simulation between $z = 2.5$ and $z = 0$ and identified the initial masses of the merging galaxies at $z = 2.5$ and their initial separation, in order to resimulate the mergers at a higher resolution. Their new simulations were done using the software Gadget 2 (Springel 2005) with galaxy models generated by the Smulders code (Smulders 1995). The resulting galaxies originated from the merger trees showed significant growth in mass ($\sim 2.2\times$) and especially in size ($\sim 4.4\times$) with respect to their compact progenitor. These results are consistent with the observed growth from $z = 2.5$ to $z = 0$. Fitting their data Tapia et al. (2013) obtained an equation that relates size and mass growth of elliptical galaxies:

$$\frac{r_{\mathrm{e,f}}}{r_{\mathrm{e,i}}} = (1.11 \pm 0.01) \left(\frac{M_{\star,\mathrm{f}}}{M_{\star,\mathrm{i}}} \right)^{(1.68 \pm 0.12)} . \tag{89}$$

This shows that the mergers with smaller satellites are the most efficient in increasing the size of the main galaxy. They also found that the velocity dispersion of the final galaxies was slightly higher than the progenitors ($\sim 1.1\times$). Other studies (Naab et al. 2009; Oser et al. 2012) found instead that there should be a decrease in the velocity dispersion of about 20%, but Tapia et al. (2013) argued that these different behaviors simply depend on the particular spatial configuration of the mergers used in each simulation.
In this chapter a re-simulation of some of the merger experiments of Tapia et al. with models generated by the new code is discussed. The Sérsic index of the progenitor galaxy is varied to investigate its influence on the process of size growth induced by dry mergers. This is an effect that has not been studied before. Two of their merger trees (MT7 and MT3 in their paper) are taken and re-simulated them three times each using three different values of the Sérsic index ($n = 1, 2, 4$), and their response to the mergers and evolution over time are compared.

6.2 Properties of the mergers

6.2.1 Properties of the initial galaxies

Following the recipe of Tapia et al. (2013), the mass of the galaxies and the spatial configuration of the mergers have been obtained identifying two merger trees in the GALFOBS project (Galaxy Formation at Different Epochs and in Different Environments: Comparison with Observational Data), a series of N-body+SPH cosmological simulations with 2^{27} luminous matter particles and 2^{27} dark matter particles. The two merger trees will be identified as A and B, and correspond to the merger trees 7 and 3 of Tapia et al. (2013), respectively. The size of the progenitor galaxies was chosen to emulate the observed compact elliptical galaxies. The size of the satellites was instead taken from the empirical law by Shen et al. (2003), which gives us the effective radius of elliptical galaxies as a function of mass:

$$\frac{r_{\rm e}}{\rm kpc} = 1.15 \left(\frac{M_\star}{10^{10} {\rm M}_\odot} \right)^{0.56}. \tag{90}$$

This formula was obtained by fitting data of early-type elliptical galaxies in the Sloan Digital Sky Survey. However, it was derived from data of the local universe, therefore it needs to be rescaled taking into account the evolution with redshift. To this purpose, we use the relation by Trujillo et al. (2006):

$$r_{\rm e}(z) = r_{\rm e} \, (1+z)^{-0.45 \pm 0.10}. \tag{91}$$

The satellites have been generated with a Sérsic index of $n = 2$, which is a realistic value for small galaxies in clusters.
All these properties are shown in Table 5 and Table 6.

6.2.2 Size of the dark halos

All the galaxies used in these simulations have a dark matter halo which follows the Hernquist profile, with mass 10 times the mass of the luminous component of the galaxy.
To choose the size of the halo have been considered several studies that evaluate the relation between the concentration c of a dark matter halo and its mass and redshift (see Coe 2010 for a review). The concentration parameter is defined as $c_{200} = r_{200}/r_{\rm NFW}$, where $r_{\rm NFW}$ is the characteristic radius of the NFW profile (Navarro et al. 1996) which best fits the halo and r_{200} is the

ID (1)	$M_\star\,(10^{11}\mathrm{M}_\odot)$ (2)	$r_\mathrm{e}\,(\mathrm{kpc})$ (3)	n (4)
Progenitor A	1.68	1.020	1,2,4
Satellite A1	0.480	1.860	2
Satellite A2	0.166	1.094	2
Satellite A3	1.661	5.189	2
Progenitor B	0.520	0.960	1,2,4
Satellite B1	0.371	1.928	2
Satellite B2	0.162	1.263	2
Satellite B3	0.527	2.625	2

Table 5: Input parameters of the initial galaxies - Col. (2): stellar mass of the galaxy. Col. (3): the effective radius, Col. (4): Sérsic index.

radius at which the average density inside it is 200 times the critical density ρ_c of the universe (i.e., the virial radius):

$$r_{200} = \left(\frac{M}{4/3\,\pi\,200\,\rho_c} \right)^{1/3} . \tag{92}$$

This allows to convert an equation for the concentration into an equation for a size parameter of the halo, r_NFW. Most of the published $c = c(M, z)$ relations are in the format $c = (A/(1+z)^B)\,M^C$ (e.g., Bullock et al. 2001). For the models in these simulations it was used the one by Duffy et al. (2008), obtained through a cosmological simulation, which is the most recent in this format:

$$c_{200} = \frac{6.71}{(1+z)^{0.44}} \left(\frac{M_\mathrm{halo}}{2 \cdot 10^{12}\,h^{-1}\,\mathrm{M}_\odot} \right)^{-0.091} . \tag{93}$$

More recent papers (e.g., Prada et al. 2012) propose a much more complicated model to determine the concentration of the halos, but in the range of mass covered by the galaxies in these simulations the results are very similar. The value of the critical density is a function of redshift, and has been calculated for a standard Λ-CDM cosmology with $H_0 = 70.4\,\mathrm{km\,s^{-1}\,Mpc^{-1}}$, $\Omega_\mathrm{d} = 0.728$, $\Omega_\mathrm{m} = 0.272$, $\Omega_\mathrm{rad} \simeq 0$, and $\Omega = 1$ (Jarosik et al. 2011):

$$\rho_c = \frac{3H_0^2}{8\pi G} \cdot (\Omega_\mathrm{d} + \Omega_\mathrm{m}\,a^{-3} + \Omega_\mathrm{rad}\,a^{-4} + (\Omega - 1)\,a^{-2}), \tag{94}$$

ID (1)	Mass ratio (2)	R_{in} (kpc) (3)	ϕ (deg) (4)	θ (deg) (5)	$v_R\,(\mathrm{km\,s^{-1}})$ (6)	$v_T\,(\mathrm{km\,s^{-1}})$ (7)
Merger Tree A						
A1	3.5	44.93	0	0	-322.45	163.43
A2	13.0	33.92	56	45	-361.40	177.11
A3	1.4	57.60	59	156	-204.46	179.66
Merger Tree B						
B1	1.4	59.90	0	0	-261.49	156.71
B2	5.5	28.29	45.31	25	-265.20	170.85
B3	2.0	34.43	55.04	128	-226.48	207.24

Table 6: Configuration of the mergers - Col. (1): identifier of the merger. Col. (2): mass ratio of the satellite with respect to the main galaxy (the remnant of the previous merger). Col. (3): initial separation between the two galaxies. Cols. (4) and (5): angles that define the position of the satellite. Cols. (6) and (7): radial and tangential velocities of the orbit of the satellite.

where $a = 1/(1+z)$ is the scale parameter of the universe. The Hernquist model with the same mass inside its half-mass radius as the NFW model up to that same radius was adopted to obtain the Hernquist parameter from corresponding to r_{NFW}. It is:

$$a_h = \left(\frac{1}{\sqrt{k}} - 1\right) r_{\mathrm{NFW}}, \tag{95}$$

where

$$k = \frac{\log 2 - \frac{1}{2}}{\log(1+c_{200}) - \frac{c_{200}}{c_{200}+1}}.$$

Putting all these equations together we obtain a relation between the Hernquist parameter of a halo and its mass and redshift, which is what has been used to generate the models.

It is worth noting that the size of the dark halos used in these simulations depends only on their mass and redshift, not on the size of the luminous component. This means that the compact primary galaxies have a very large dark matter halo relatively to their size. This is realistic if we imagine that these galaxies have shrunk to their current size by gas friction, which does not affect the halo. For comparison, in the simulations of Tapia et. al (2013)

all the galaxies had a dark matter halo about 5 times larger in size than the luminous component.

6.2.3 Computational details

The models used to represent the galaxies are all two-components isotropic models, with a Prugniel-Simien luminous component and a Hernquist dark matter halo.
The number of particles of each galaxy has been selected so that in each merger tree they all have the same mass per particle: $3.35 \cdot 10^6\,\mathrm{M}_\odot$ in Merger Tree A and $1.04 \cdot 10^6\,\mathrm{M}_\odot$ in Merger Tree B for luminous matter, and twice as much for dark matter ($2.08 \cdot 10^6\,\mathrm{M}_\odot$ and $6.70 \cdot 10^6\,\mathrm{M}_\odot$, respectively).
This way the progenitor galaxies have 50000 luminous particles and the satellites have an amount of particles scaled according to their mass. The total number of particles in each Merger Tree is about 750000, of which about 200000 of luminous matter.
The unit conversion between the internal units of the simulations and the physical units shown in the paper is the following: [L]=0.8 kpc, [M]=$10^{12}\,\mathrm{M}_\odot$, [T]=0.34 Myr, [V] = $2318.14\,\mathrm{km\,s^{-1}}$.
All the models have been left evolving in isolation before the mergers, to make sure that they are stable. The input parameters of the code have been tweaked so that the resulting galaxies have the properties shown in Table 5 after relaxation.
All the simulations, including the relaxation of the initial models, were carried out with the code Gadget 2 (Springel 2005), setting a softening length of 16 pc for the luminous matter and 32 pc for the dark matter. The softening length for dark matter is twice as big to compensate for the bigger particle mass. Each of the simulated merger events has been carried out indipendently, waiting for the galaxies to be fully merged before beginning the next merger; almost all of the mergers were over after 6000 internal time units (about 2 Gyr).

6.2.4 Measuring methods

All the measurements of effective radius, mass and integrated line-of-sight velocity dispersion are averages of 30 random projections of the system onto different planes. For each of these projections the mass has been obtained by counting the number of particles in concentric rings out to where the

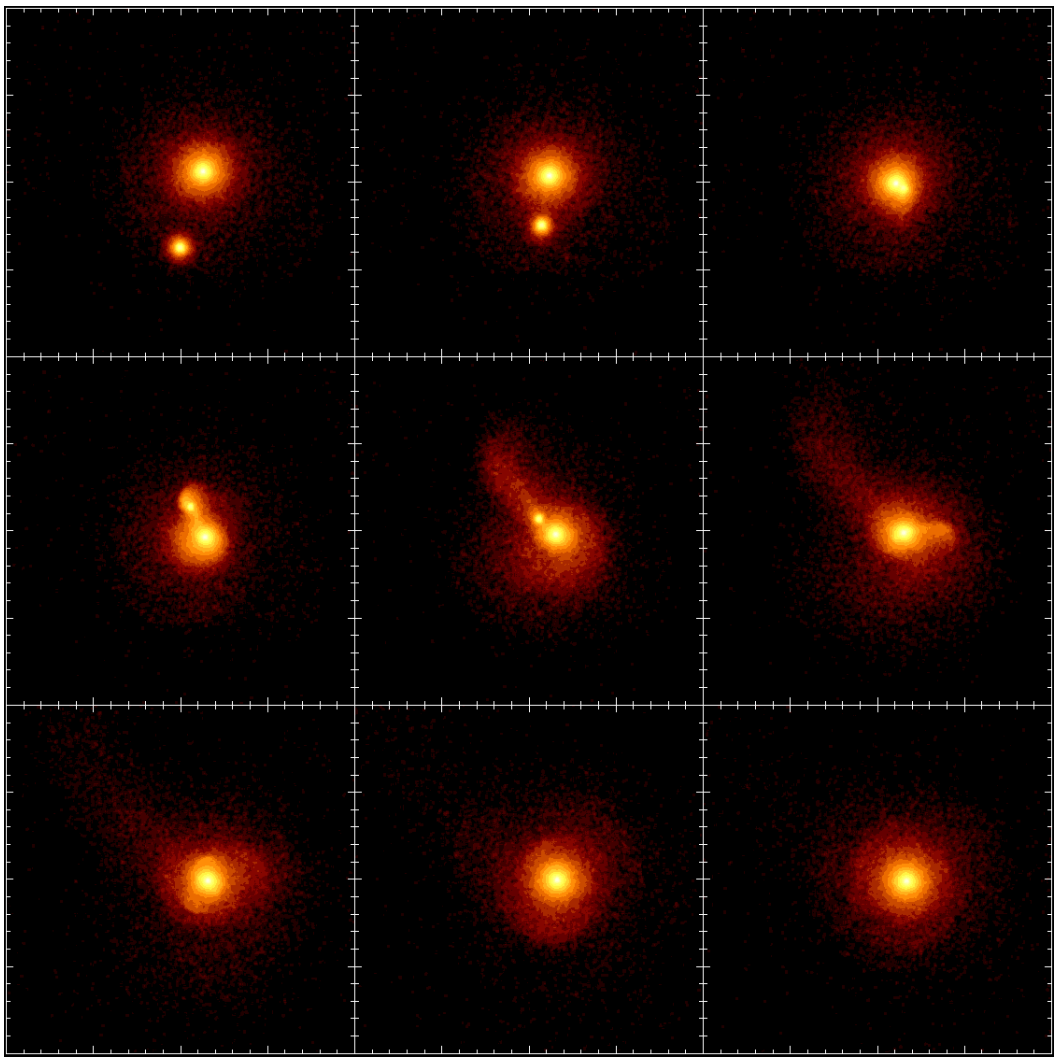

Figure 15: Snapshots of the second merger of Merger Tree B. From left to right and top to bottom the snapshots were taken respectively at time: 0 Myr, 34 Myr, 68 Myr, 102 Myr, 170 Myr, 238 Myr, 340 Myr, 510 Myr and 680 Myr from the beginning of the merger. Each plot has a size of $160 \times 160\,\mathrm{kpc}^2$.

galaxy is 6 magnitudes less bright than the center. The effective radius is the radius inside which lies half of this truncated mass. The velocity dispersion is the average velocity dispersion inside this effective radius. The 6 magnitudes criterium was adopted to mimic the fact that in real observations

the outermost parts of the galaxy are too faint to be detected, and to exclude tidal structures resulting from mergers. The fits of the surface brightness profiles with a Sérsic law are non-weighted fits in the range 0.08 to 80 kpc, carried out with a routine written on purpose which uses the Levenberg-Marquardt method for non-linear regression (see Press et al. 1986, Chapter 15.5).
After each phase of the merger trees the particles which escaped more than 80 kpc from the center were cut out of the next simulation, because they would not have had any influence in the next simulation and would have just slowed it down.

6.3 Results

Each merger tree is composed of 3 successive mergers. Each of them starts with the infalling satellite at a distance of 30 to 60 kpc from the main galaxy, which is at least ~ 10 times its effective radius. The satellite is thus mostly outside the luminous matter distribution of the main galaxy, but still inside its dark matter halo. Figure 15 shows an example of how the mergers unfold, relative to the second merger of Merger Tree B. The merger is seen from above the orbital plane of the two galaxies. The first passage through the pericenter occurs between frames 3 and 4, about ~ 75 Myr from the beginning of the merger. During this passage the satellite begins to get disrupted by the gravitational field of the main galaxy, and material from the external parts of the main galaxy gains energy and goes into new, wider orbits, making the overall effective radius bigger. The nuclei of the two galaxies are merged after ~ 250 Myr (Fig. 15, frame 6), and it takes 400 more Myr for the galactic matter to settle on a circularly-symmetric distribution (Fig. 15, frame 9).
Table 7 shows the physical properties of the main galaxy during the various stages of the mergers and for each merger tree. The data obtained in Tapia et al. (2013) for the corresponding merger trees is also shown for comparison. In each case the surface-brightness radial profile is fitted with a Sérsic law, and the resulting Sérsic index is shown in the table. The ${\chi_\nu}^2$ value of the Sérsic law fit is also indicated as a measure of how well the data is represented by this law. Despite the large deviations from it, the Sérsic law is always adopted to fit the models because observations show that the surface brightness of elliptical galaxies follows it. Comparing the surface brightness of the models with the Sérsic law is thus a way of comparing these simulations to the observations of real galaxies.

MT (1)	ID (2)	$M_\star\,(10^{11}\mathrm{M}_\odot)$ (3)	r_e (kpc) (4)	n (5)	${\chi_\nu}^2$ (6)	$\sigma_\mathrm{e}\,(\mathrm{km\,s^{-1}})$ (7)
$A, n = 1$	0	1.656	1.020	1.06	1.23	309.23
	1	1.881	1.219	3.93	194.46	308.11
	2	2.002	1.495	3.59	164.55	308.87
	3	3.818	4.780	3.30	101.58	282.19
$A, n = 2$	0	1.633	1.020	1.94	1.87	313.00
	1	1.948	1.319	4.39	82.30	308.00
	2	2.054	1.562	4.35	81.16	303.07
	3	3.833	5.032	4.22	84.97	283.75
$A, n = 4$	0	1.583	1.020	4.09	2.88	330.12
	1	1.982	1.520	5.44	20.27	314.40
	2	2.109	1.787	6.02	14.24	311.89
	3	3.846	5.442	6.34	124.85	283.21
$B, n = 1$	0	0.512	0.960	0.99	1.70	179.90
	1	0.778	1.556	3.60	147.14	184.12
	2	0.927	2.093	3.68	136.24	181.13
	3	1.470	3.978	3.28	96.89	180.78
$B, n = 2$	0	0.507	0.960	1.94	2.09	181.48
	1	0.812	1.803	4.13	57.94	182.26
	2	0.944	2.380	4.29	61.86	179.74
	3	1.468	4.097	4.04	48.07	180.82
$B, n = 4$	0	0.487	0.960	3.88	1.06	191.00
	1	0.823	2.272	6.80	6.40	186.18
	2	0.958	3.027	7.82	9.56	181.81
	3	1.475	4.619	7.16	38.29	181.73
Tapia A	0	1.48	1.02	...	...	414.48
	3	3.63	5.75	...	...	412.40
Tapia B	0	0.45	0.96	...	...	231.35
	3	1.46	6.74	...	...	275.86

Table 7: Physical properties of the main galaxy after each stage of each merger tree. Col. (1): identifier of the merger tree. Col. (2): stage of the main galaxy (0=progenitor galaxy, 1=remnant of the first merger, 2=remnant of the second merger, 3=final remnant). Cols. (3), (4), (5), (6), and (7): stellar mass, effective radius, Sérsic index, reduced ${\chi_\nu}^2$ of the Sérsic law fit, and average velocity dispersion within the effective radius, respectively.

- **Size growth:** The effective radius gets bigger as expected, and the ratio of the increase is compatible with the one between local and compact elliptical galaxies at $z \sim 2$. However, it is somewhat smaller than what Tapia et al. (2013) found, possibly because of the relative instability of the models generated from the Smulders code. Figures 16 and 17 show the radial profile of surface mass density (which assuming a constant mass-to-light ratio is proportional to surface brightness) and of velocity dispersion of the final galaxy of each Merger Tree. The profile of the final galaxy is compared with the profiles of the progenitor and satellite components, as well as with the profile of the progenitor before the mergers. The figures show that the matter from the satellites dominates in the outer parts of the final galaxy, despite being several orders of magnitudes less dense than the core, and that the core of the progenitor is mostly unaffected. This suggests that the size growth is mostly determined by the accretion of matter from the satellites in the outer parts of the primary galaxy. However, there is definitely a weak dependence on the Sérsic index of the progenitor galaxy. One might think this is because as the satellites plunge into the progenitor they get disrupted when the density of the progenitor becomes greater than their own, depositing their matter at that distance. This distance would thus depend on the density of the progenitor, and therefore its Sérsic index. However, this is not the case for these simulations. The satellites do not reach the core. In fact inside $r \sim 0.1\,\mathrm{kpc}$ there are no particles from the satellites, and their density drops to 0. They deposit their matter at the same distance from the center and with the same distribution, regardless of the Sérsic index of the primary galaxy. This can be seen in Figure 18, which for each satellite of Merger Tree A compares the the surface mass density in the three cases with $n = 1, 2, 4$. Most likely this distance is related to the orbital angular momentum of the satellites, which keeps them from falling in the center where the different Sérsic index would have made a difference. The observed difference in effective radius is instead due to the outer parts of the progenitor, which gain energy from the merger and move to higher orbits. The Sérsic profiles with higher n are denser in the outskirts, and therefore undergo a bigger expansion. This can be seen in Figures 16 and 17 by comparing the distribution of matter of the progenitor before and after the mergers. The center of the progenitor also undergoes an expansion, but this is probably related to the time evolution software.

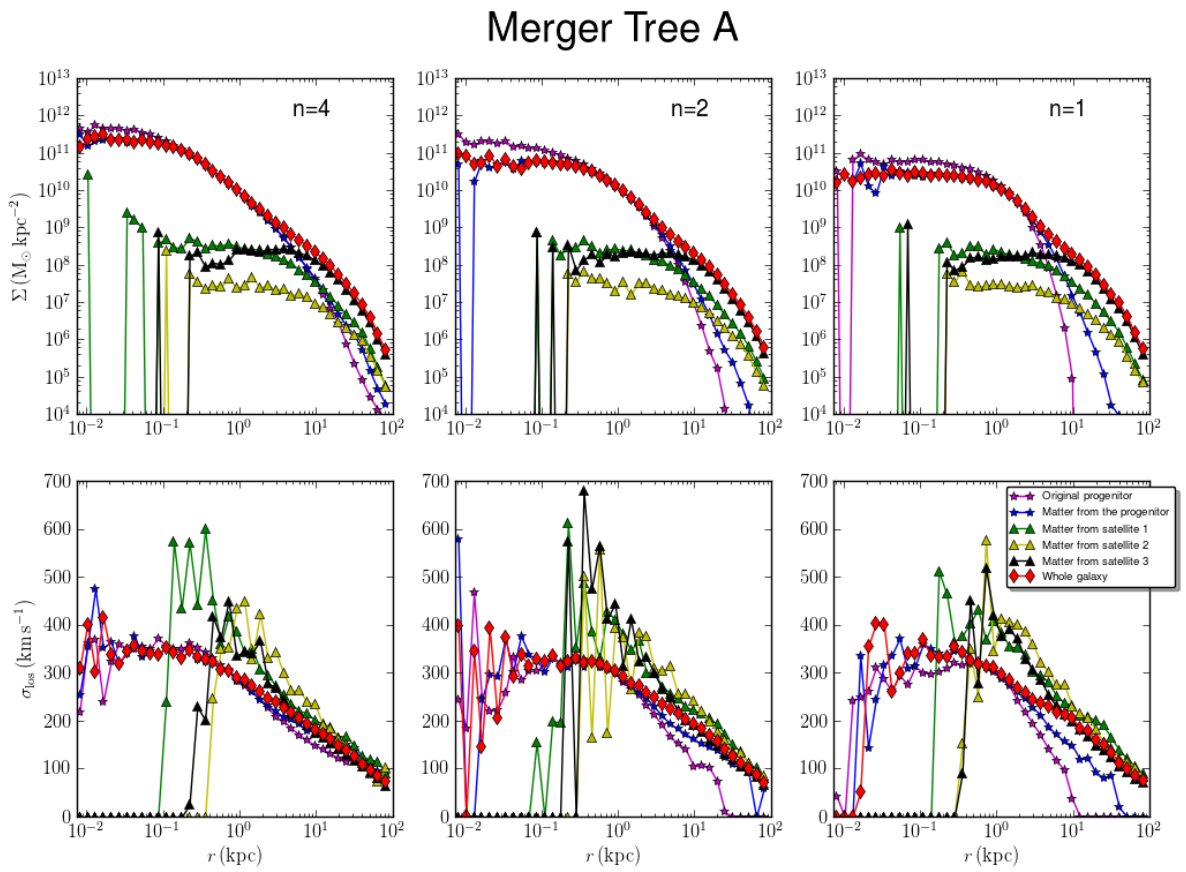

Figure 16: Upper panels: Surface mass density profile of the final galaxy of Merger Tree A in the three cases ($n = 1, 2, 4$) compared to the contributions from the progenitor and each satellite. The surface brightness of the original progenitor (before the mergers) is also shown for comparison. Lower panels: line of sight velocity dispersion profile for the final galaxy and its separated components.

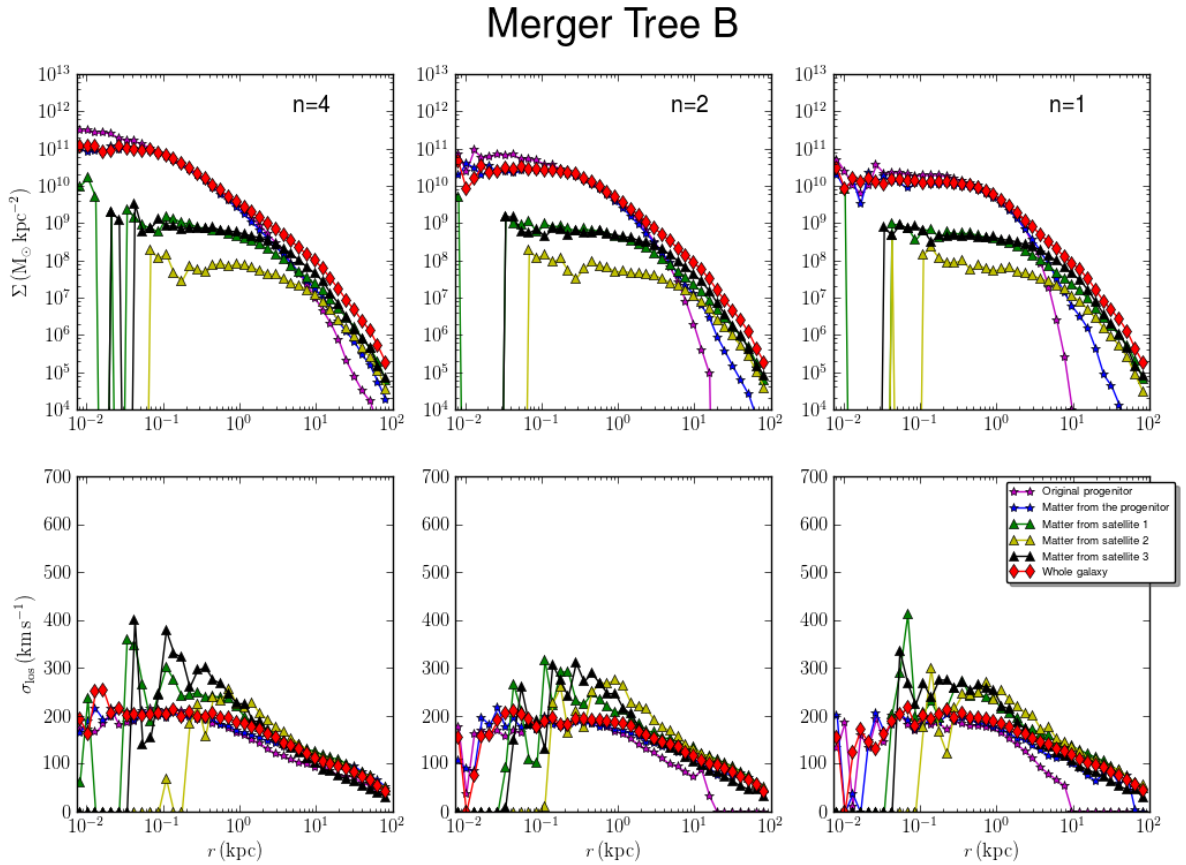

Figure 17: As in Figure 16 but for Merger Tree B.

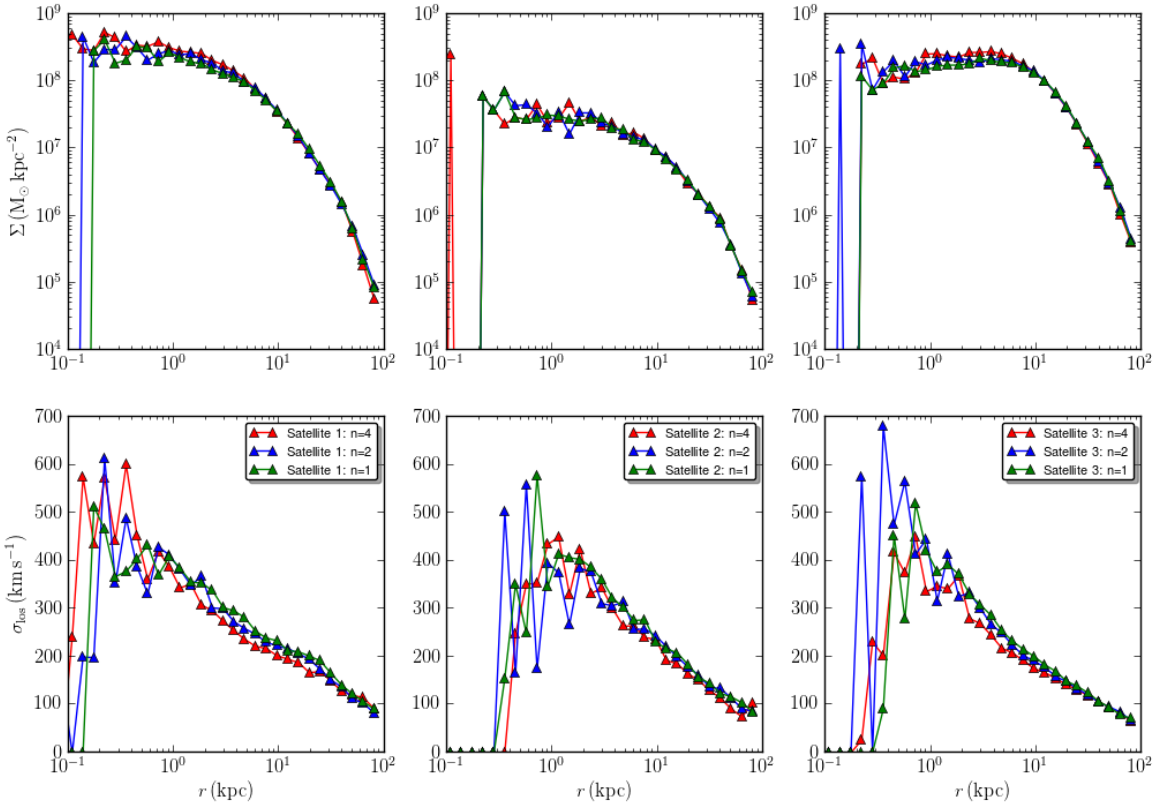

Figure 18: Upper panels: Comparison of the contributions of each satellite to the surface mass density profile of the final galaxy of Merger Tree A in the three cases ($n = 1, 2, 4$). Lower panels: As in the top panels but for the line of sight velocity dispersion.

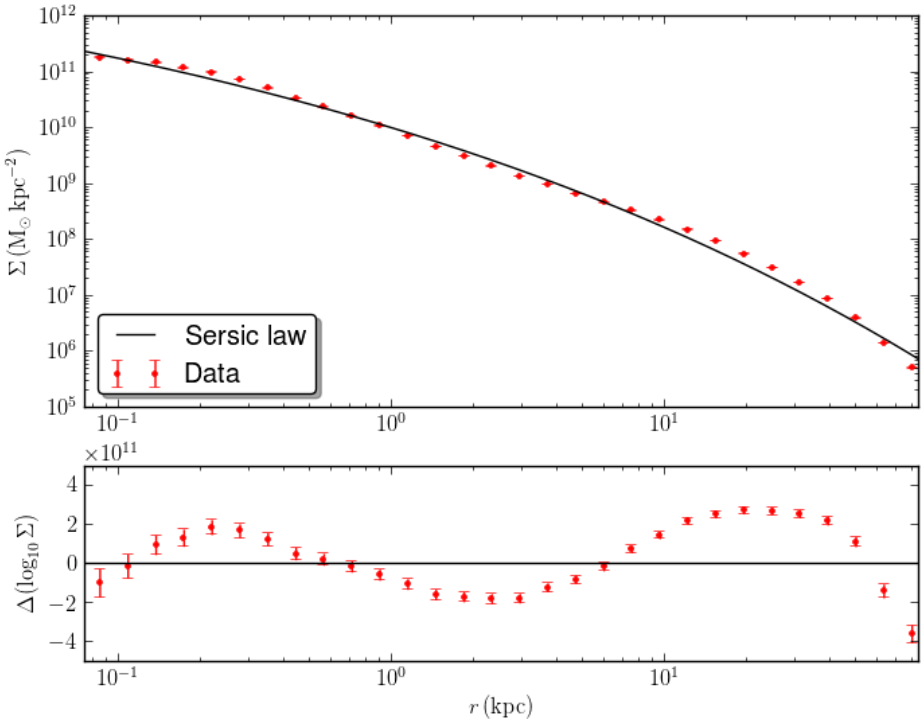

Figure 19: Fitting with a Sérsic law of the remnant galaxy of the Merger Tree A with $n = 4$. The result of the fit is $n = 6.345$ with ${\chi_\nu}^2 \sim 125$.

- **Sérsic index of the remnant galaxy:** The Sérsic index of the main galaxy grows by a factor of about 2, which depends on the initial Sérsic index. The growth mostly happens in the first merger, after which it does not change much. However, from Table 7 it is evident that the remnant galaxies are not very well fitted by the Sérsic law, having very high ${\chi_\nu}^2$ values. Figure 19 shows the surface brightness of the remnant galaxy of the $n = 4$ case fitted with a Sérsic law, and the residuals of the fit. The plot shows that there is an excess of mass at certain radii, probably resulting from the satellites depositing there most of their mass. Despite this, it is notable how the Sérsic index appears to tend towards $n \geq 4$, which is the expected index for a massive elliptical galaxies.

- **Velocity dispersion:** The average line-of-sight velocity dispersion is slightly decreasing by a factor of 5%. This is different from the small increase found in Tapia et al. (2013). This decrease appears to be most important for larger Sérsic indices. For the $n = 4$ case the decrease is of the order of 10%, which is more in agreement with what was found by Naab et al. (2009) and Oser et al. (2012). Interestingly, the final velocity dispersion approaches the same value for every n. It is $283\,\mathrm{kms}^{-1}$ for Merger Tree A and $181\,\mathrm{kms}^{-1}$ for Merger Tree B.
  The lower panels of Figures 16 and 17 gives us a more complete picture by comparing the velocity dispersion radial profiles of the overall final galaxy with the one of its separate components. The matter from the satellites shows a higher velocity dispersion at intermediate radii, $r \sim 1\,\mathrm{kpc}$. This means that the satellites were disrupted further out and that their matter is on orbits that reach out to larger radii than the matter of the progenitor at similar radii. In all considered cases the matter from the progenitor has a higher velocity dispersion in the outer parts than the before the mergers. This is due to the kinetic energy gained from the satellites (tidal heating). In the inner parts instead the velocity dispersion profile of the progenitor is left almost untouched, with the exception of the case with $n = 1$ of Merger Tree A. While in the other cases the high central density and strong gravitational potential make them insensitive to the mergers in the outer parts, it appears that in the case A with $n = 1$ the satellites were able to trasfer some energy to the core. However, the small number of particles in the center makes the velocity dispersion oscillate a lot, which makes it harder to analyze.

Figure 20 and Table 8 summarize the variation in size, mass, velocity dispersion and Sérsic index due to the process of dry mergers.

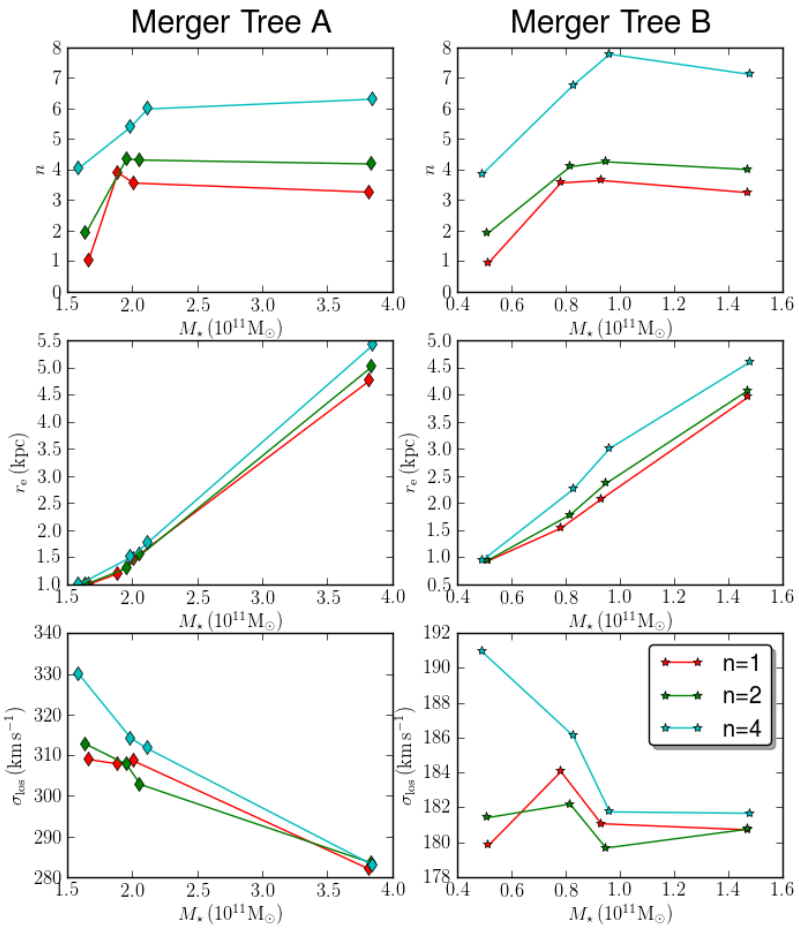

Figure 20: Upper panels: Sérsic index of the main galaxy as a function of stellar mass in each stage of each merger tree. Middle panels: effective radius as a function of stellar mass. Lower panels: average line-of-sight velocity dispersion as a function of stellar mass.

MT (1)	$f_{M_\star}$ (2)	f_{r_e} (3)	f_{σ_e} (4)	f_n (5)
$A, n = 1$	2.305	4.686	0.912	3.117
$A, n = 2$	2.347	4.933	0.906	2.178
$A, n = 4$	2.429	5.335	0.858	1.552
Tapia et al. A	2.45	5.65	0.99	...
$B, n = 1$	2.871	4.144	1.005	3.320
$B, n = 2$	2.895	4.68	0.996	2.081
$B, n = 4$	3.029	4.811	0.951	1.844
Tapia et al. B	3.27	7.02	1.19	...

Table 8: Variation of the physical properties of the progenitor galaxy after the mergers. Col. (1): identifier of the merger tree. Cols. (2), (3), (4) and (5): increase in mass, effective radius, velocity dispersion, and Sérsic index of the final remnant with respect to the progenitor.

7 Conclusions

The code described in this thesis successfully generates numerical models of spherical galaxies that follow the Sérsic law. This allows to represent a wide range of elliptical galaxies, from dwarf ellipticals to giant ones. The adoption of the Sérsic law is a significant improvement over the older code by Smulders (1995), which instead generated models following the de Vaucouleurs law, accurate only for the representation of very large elliptical galaxies. Additionally the new code allows the user to select more parameters, and its models are more accurate and stable. Numerical simulations that employ models created with this code can be used to study an extensive range of scientific problems, such as formation processes, dark matter content and distribution, internal structure, dynamical instability, and scaling laws. While the study of these phenomena can be approached by analytical means, only numerical simulations allow a complete description.
One such numerical study has been presented in this thesis, which will be extended in a paper to be published in late 2014. The main results and future developments can be summarized as follows:

- The merger experiments show that, through the process of dry mergers with smaller satellites, compact elliptical galaxies can significantly grow in size, by a factor $\sim 4.8\times$, and in mass, by a factor $\sim 2.5\times$. The velocity dispersion suffers a slight decrease in the process, up to 10%. The Sérsic index of the final galaxy is significantly larger than the initial one, and in most of the examined cases it is larger than 4. These results therefore support the hypothesis that the compact elliptical galaxies observed at $z \sim 2$ are the progenitors of the giant elliptical galaxies of the local universe, and that dry mergers with satellites are the primary cause of this size growth.

- According to the results the dependence on the Sérsic index of this growth process is weak. The matter from the satellite galaxies does not reach the compact core of the progenitor, where the different density profiles would have made a significant difference. The most relevant factors are instead the mass and orbital angular momentum of the satellite galaxies. However, this was a small sample of merger trees, and more simulations might further clarify the picture. In different cases of galaxy formation processes the Sérsic index might prove more relevant,

for instance when the difference in density between the progenitor and the satellites is smaller.

- The surface brightness of remnant galaxies after the mergers does not exhibit a clear Sérsic law behaviour. With more simulations, it would be interesting to be able to link specific patterns in the surface brightness radial profile of the final galaxy to its formation process. It is also worth investigating and understanding how the uniform Sérsic laws that we observe in real galaxies do arise after their formation processes.

References

Baes, M. ,& Gentile, G. 2011, A&A, 525, A136
Barnes, J. ,& Efstathiou, G. 1987, ApJ, 319, 575
Bernardi, M., Sheth, R. K., Annis, J., et al. 2003, AJ, 125, 1817
Bernardi, M., Sheth, R. K., Nichol, R. C., et al. 2006, AJ, 131, 2018
Binney, J., & Tremaine, S. 1987, Galactic Dynamics (NJ: Princeton Univ. Press)
Buitrago, F., Trujillo, I., Conselice, C. J., et al. 2008, ApJ, 687, L61
Bullock, J. S., Kolatt, T. S., Sigad, Y., et al. 2001, MNRAS, 321, 559
Burkert, A. 1993, A&A, 278, 23
Caon, N., Capaccioli, M., & D'Onofrio, M. 1993, MNRAS, 265, 1013
Carrol, B. W., & Ostlie, D. A. 1996, An Introduction to Modern Astrophysics (Reading, MA: Addison-Wesley Publishing)
Ciotti, L. 1996, ApJ, 471, 68
Coe, D. 2010, arXiv:1005.0411
Cooper, M. C., Griffith, R. L., Newman, J. A., et al. 2012, MNRAS, 419, 3018
Curtis, H. D. 1918, Pub. Lick Obs. XIII, 11
Daddi, E., Renzini, A., Pirzkal, N., et al. 2005, ApJ, 626, 680
de Vaucouleurs, G. 1948, Ann. Ap., 11, 247
de Vaucouleurs, G. 1953, MNRAS, 113, 134
de Vaucouleurs, G. 1959, Hand. Phys., 53, 275
Devroye, L. 1986, Non-uniform Random Variate Generation (New York, NY: Springer-Verlag)
Djorgovski, S., & Davis, M. 1987, ApJ, 313, 59
Dressler, A. 1980, ApJ, 236, 351
Dressler, A., Lynden-Bell, D., Burstein, D., et al. 1987, ApJ, 313, 42
Duffy, A. R., Schaye, J., Kay, S. T., & Dalla Vecchia, C. 2008, MNRAS, 390, L64
Ferré-Mateu, A., Vazdekis, A., Trujillo, I., et al. 2012, MNRAS, 423, 632
Gerhard, O. 2006, in ESO Astrophysics Symposia, Planetary Nebulae Beyond the Milky Way, ed. L. Stanghellini, J. R. Walsh, & N. G. Douglas (Berlin: Springer-Verlag), 299
González-García, A. C., & van Albada, T. S. 2003, MNRAS, 342, 36
Hernquist, L. 1990, ApJ, 356, 359
Herschel, W. 1864, Phil. Trans. Royal S. London, 154, 1
Hubble, E. 1922, ApJ, 56, 162

Hubble, E. 1925, Obs., 48, 159
Hubble, E. 1926, ApJ, 64, 321
Jaffe W. 1983, MNRAS, 202, 995
Jarosik, N., Bennett, C. L., Dunkley, J., et al. 2011, ApJS, 192, 14
Kormendy, J., & Bender, R. 1996, ApJ, 464, L119
Kormendy, J., Fisher, D. B., Cornell, M. E., & Bender, R. 2009, ApJS, 182, 216
Mellier, Y., & Mathez, G. 1987, A&A, 175, 1
Merritt, D. 1985, AJ, 90, 1027
Morgan, W. W. 1958, PASP, 70, 364
Naab, T., Johansson, P. H., & Ostriker J. P. 2009, ApJ, 699, L178
Navarro, J., Frenk, C. S., & White, S. D. M. 1996, ApJ, 462, 563
Oser, L., Naab, T., Ostriker, J. P., & Johansson, P. H. 2012, ApJ, 744, 63
Osipkov, L. P. 1979, Pis'ma v Atron. Zhur., 5, 77
Prada, F., Klypin, A. A., Cuesta, A. J., Betancort-Rijo, J. E., et al. 2012, MNRAS, 423, 3018
Press, W. H., Teukolsky, S. A., Vetterling, W. T., et al. 1986, Numerical Recipes in Fortran 77: The Art of Scientific Computing (Cambridge: Cambridge Univ. Press)
Prugniel, P., & Simien, F. 1997, A&A, 321, 111
Roberts, I. 1893, A Selection of Photographs of Stars, Star-clusters and Nebulae (London: The Universal Press)
Sandage, A. 1961, The Hubble Atlas of Galaxies (Washington, DC: Carnegie Institution)
Sandage, A., & Bedke, J. 1994, The Carnegie Atlas of Galaxies (Washington, DC: Carnegie Institution)
Sérsic, J. L. 1963, Bol. As. Argentina Astron., 6, 41
Smulders, M. 1995, M.Sc. Thesis, University of Groningen
Springel, V. 2005, MNRAS, 364, 1105
Terzić, B. & Graham, A. W. 2005, MNRAS, 362, 197
Tapia, T., Balcells, M., González-García, A. C., et al. 2013, in Highlights of Spanish Astrophysics VIII, X Scientific Meeting of the Spanish Astronomical Society, ed. J. C. Guirado, L. M. Lara, V. Quilis, & J. Gorgas (Barcelona: SEA), 418
Trujillo, I., Feulner, G., Goranova, Y., et al. 2006, ApJ, 650, 18
Trujillo, I., Conselice, C. J., Bundy, K., et al. 2007, MNRAS, 382, 109
Trujillo, I., Cenarro, A. J., de Lorenzo-Cáceres, A., et al. 2009, ApJ, 692, L118

Trujillo, I., Ferreras, I., & de La Rosa, I. G. 2011, MNRAS, 415, 3903
van den Bergh, S. 1976, ApJ, 206, 883
van Dokkum, P. G., Franx, M., Kriek, M., et al. 2008, ApJ, 677, L5
van Dokkum, P. G., Whitaker, K. E., Brammer, G., et al. 2010, ApJ, 709, 1018